Complex refractive indices and single scattering albedo of global dust aerosols in the shortwave spectrum and relationship to ~~size and~~ iron content ~~and size~~

Claudia Di Biagio[1], Paola Formenti[1], Yves Balkanski[2], Lorenzo Caponi[1,3], Mathieu Cazaunau[1], Edouard Pangui[1], Emilie Journet[1], Sophie Nowak[4], Meinrat O. Andreae[5,6], Konrad Kandler[7], Thuraya Saeed[8], Stuart Piketh[9], David Seibert[10], Earle Williams[11], and Jean-Francois Doussin[1]

[1] *LISA, UMR CNRS 7583, Université Paris–Est–Créteil, Université de Paris, Institut Pierre Simon Laplace (IPSL), Créteil, France* ~~Laboratoire Interuniversitaire des Systèmes Atmosphériques (LISA), UMR7583, CNRS, Université Paris Est Créteil et Université Paris Diderot, Institut Pierre et Simon Laplace, Créteil, France~~

[2] *Laboratoire des Sciences du Climat et de l'Environnement, CEA CNRS UVSQ UP Saclay, 91191, Gif sur Yvette, France*

[3] *PM_TEN srl, Piazza della Vittoria 7/14, 16121, Genoa, Italy*

[4] *Plateforme RX UFR de chimie, Université Paris Diderot, Paris, France*

[5] *Max Planck Institute for Chemistry, P.O. Box 3060, 55020, Mainz, Germany* ~~Biogeochemistry Department, Max Planck Institute for Chemistry, P.O. box 3060, 55020, Mainz, Germany~~

[6] *Geology and Geophysics Department, King Saud University, Riyadh, Saudi Arabia*

[7] *Institut für Angewandte Geowissenschaften, Technische Universität Darmstadt, Schnittspahnstr. 9, 64287 Darmstadt, Germany*

[8] *Science Department, College of Basic Education, Public Authority for Applied Education and Training, Al-Ardeya, Kuwait*

[9] *Climatology Research Group, Unit for Environmental Science and Management, North-West University, Potchefstroom, South Africa*

[10] *Walden University, Minneapolis, Minnesota, USA*

[11] *Parsons Laboratory, Massachusetts Institute of Technology, Cambridge, Massachusetts, USA*

Correspondence to: C. Di Biagio (claudia.dibiagio@lisa.u-pec.fr)

Abstract

The optical properties of airborne mineral dust depend on its mineralogy, size distribution, and shape, and might vary between different source regions. To date, large differences in refractive index values found in the literature have not been fully explained. In this paper we present a new dataset of complex refractive indices (m=n–ik) and single scattering albedos (SSA) for 19 mineral dust aerosols over the 370–950 nm range in dry conditions. Dust aerosols were generated from natural parent soils from eight source regions (Northern Africa, Sahel, Middle East, Eastern Asia, North and South America, Southern Africa, and Australia). They~~se~~ were selected to represent the global scale variability of the dust mineralogy. Dust was re–suspended into a 4.2 m^3 smog chamber where its spectral shortwave scattering (β_{sca}) and absorption (β_{abs}) coefficients, number size distribution, and bulk composition were measured. The complex refractive index was estimated by Mie calculations combining optical and size data, while the spectral SSA was directly retrieved from β_{sca} and β_{abs} measurements. Dust is assumed to be spherical in the whole data treatment, which introduces a potential source of uncertainty. Our results show that the imaginary part of the refractive index (k) and the SSA ~~largely~~ vary widely from sample to sample, with values for k in the range 0.001~~1~~ to 0.00~~9~~88 at 370 nm, 0.0006 to 0.0048 at 520 nm, and 0.0003 to

46   0.002~~1~~ at 950 nm, and values for SSA in the range 0.70 to 0.96 at 370 nm, 0.85 to 0.98 at 520 nm, and

47   0.95 to 0.99 at 950 nm. In contrast, the real part of the refractive index (n) is mostly source (and wave-

48   length) independent, with an average value between 1.48 and 1.55. The sample–to–sample variability

49   in our dataset of k and SSA is mostly related to differences in the dust's iron content. In particular, a

50   wavelength–dependent linear relationship is found between the magnitude of k and SSA and the mass

51   concentrations of both iron oxide and total elemental iron, with i~~-~~ron oxide better correlated than total

52   elemental iron to both k and SSA. ~~As an intrinsic property of matter,~~ The value of k was found to be~~is~~

53   independent of size. When the iron oxide content exceeds ~~>~~3%, the SSA linearly decreases with in-

54   creasing fraction of coarse particles at short wavelengths (< 600 nm).

55   Compared to the literature, our values for the real part of the refractive index and SSA are in line with

56   past results, while we found lower values of k compared to most of the literature values currently used

57   in climate models

58   We recommend that source–dependent values of the SW spectral refractive index and SSA ~~are~~be used

59   in models and remote sensing retrievals instead of generic values. In particular, the close relationships

60   found between k or ~~/~~SSA and the iron content in dust enable establishing predictive rules for spectrally–

61   resolved SW absorption based on particle composition.

62

63   **Introduction**

64   With teragram amounts of annual emissions, a residence time of about 1–2 weeks in the atmosphere,

65   and a planetary–scale transport, mineral dust aerosols are a global phenomenon (Uno et al., 2009;

66   Ginoux et al., 2012), and contribute significantly to the global and regional aerosol loading (Ridley et

67   al., 2016) and direct radiative effect (Miller et al., 2014).

68   However, large uncertainties still persist on the magnitude and overall sign of the dust direct radiative

69   effect (Boucher et al., 2013; Highwood and Ryder, 2014; Kok et al., 2017). One of the major sources of

70   this uncertainty is our insufficient knowledge of the dust's absorption properties in the shortwave (SW)

71   and longwave (LW) spectral ranges (e.g., Balkanski et al., 2007; Samset et al., 2018), given that mineral

72   dust contains large particles and a variety of minerals absorbing over both spectral regions (e.g. iron

73   oxides, clays, quartz and calcium–rich species;~~,~~ Sokolik and Toon, 1999; Lafon et al., 2006; Di Biagio

74   et al., 2014a, b). Global and regional scale mapping of dust absorption remains limited and more infor-

75   mation is required (Samset et al., 2018).

76   Aerosol absorption is represented both by the imaginary part (k) of the complex refractive index (m=n–

77   ik) of its constituent material, and by the single scattering albedo (SSA, i.e., the ratio of the scattering

78   to extinction coefficient) of the particle population, as well as by the mass absorption efficiency (MAE,

79   units of $m^2\ g^{-1}$), i.e., the aerosol absorption coefficient per unit ~~of aerosol~~ mass concentration.

80   In the shortwave spectral range, absorption by dust accounts for up to ~10–20% of its total extinction.

81   Dust absorption is highest in the UV–VIS, and almost nil towards the near IR (Cattrall et al., 2003;

82   Redmond et al., 2010), due to the combined contribution of large particles in the size distribution and

83   the dust's mineralogy, notably the presence of iron oxides (Karickhoff and Bailey, 1973; Lafon et al.,

84 2006; Derimian et al., 2008; Moosmüller et al., 2012; Formenti et al., 2014a; 2014b; Engelbrecht et al.,
85 2016; Caponi et al., 2017). The mineralogy of airborne mineral dust varies according to that of the
86 parent soils (Nickovic et al., 2012; Journet et al., 2014). Consequently, dust aerosols of different origins
87 should be more or less absorbing in the SW, and have different imaginary spectral refractive index and
88 SSA. Field and laboratory measurements, including ground–based and space–borne remote sensing,
89 show that k varies at a regional scale by almost two orders of magnitude (0.0001–0.008 at 550 nm) with
90 corresponding SSAs between 0.80 and 0.99 at 550 nm (Volz 1972; Patterson et al., 1977; Shettle and
91 Fenn, 1979; Dubovik et al., 2002; Haywood et al., 2003; Sinyuk et al., 2003; Linke et al., 2006; Osborne
92 et al., 2008; Müller et al., 2009; Otto et al., 2009; Petzold et al., 2009; Schladitz et al., 2009; McConnell
93 et al., 2010; Formenti et al., 2011; Wagner et al., 2012; Ryder et al., 2013a; Engelbrecht et al., 2016;
94 Rocha- Lima et al., 2018). Albeit some variability being instrumental or analytical (differences in the
95 sampled size fraction or in the method used to retrieve optical parameters), geographic differences
96 persist when the same measurement approach and retrieval method are applied, e.g., in AERONET
97 inversions, supporting the dependence of dust k and SSA with locationits origin (Dubovik et al., 2002;
98 Koven and Fung, 2006; Su and Toon, 2011). In contrast, the real part (n) of the dust refractive index,
99 mostly related to particle scattering, is estimated to be less variable than the imaginary part, with values
100 between 1.47–1.56 at 550 nm (i.e.g., Volz, 1972; Patterson et al., 1977; Balkanski et al., 2007; Petzold
101 et al., 2009).

102 Differences in k or SSA caused by the spatial variability of the iron content may affect the sign of the
103 dust radiative effect (heating vs cooling) (Liao and Seinfeld, 1998; Claquin et al. 1999; Miller et al.,
104 2014), and its global and regional implications (Myhre and Stordal, 2001; Colarco et al., 2014; Das et
105 al., 2015; Jin et al., 2016; Bangalath and Stenchikov, 2016; Strong et al., 2018). For instance, various
106 studies suggest that tThe direct radiative effect of dust has a strong impact on the Western African
107 Monsoon (Yoshioka et al., 2007; Konaré et al., 2008) and the Indian Summer Monsoon (Vinoj et al.,
108 2014; Das et al., 2015; Jin et al., 2016). However, there is no consensus whether dust increases or
109 decreases precipitation over these regions (Solmon et al., 2008; Jin et al., 2016; Strong et al., 2018).
110 As an example, Solmon et al. (2008) indicate that dust reduces precipitation over most of the Sahelian
111 region, but increases it over the Northern Sahel–Southern Sahara. This pattern is, however, very sen-
112 sitive to the dust absorbing properties, and a decrease of few percent in dust absorption may even
113 cancel out the increase of precipitation over the Sahel. Similarly, Jin et al. (2016) show that by varying
114 k from zero to 0.008 at 600 nm (i.e., the highest value currently used in models) the dust effect on the
115 Indian Summer Monsoon may shift from negative (reduction of precipitation) to positive (increase of
116 precipitation) values.

117 In spite of this sensitivity, present climate models adopt a globally–constant spectral complex refractive
118 index (and SSA) for dust, and hence still implicitly assume the same dust mineralogical composition at
119 the global scale. This is mainly due to the lack of a globally consistent dataset providing information of
120 the geographical variability of the dust scattering and absorption properties (e.g., Sunset et al., 2018).
121 Reference values for the refractive index are usually taken from Volz (1972), Patterson et al. (1977),
122 D'Almeida et al. (1991), Shettle and Fenn (1979), Sokolik et al. (1993), Sinyuk et al. (2003), or OPAC
123 (Hess et al., 1998; Koepke et al., 2015). A parameterization of the spectrally–resolved dust refractive

124 index as a function of the mineralogical composition of the particles is desirable to replace the globally

125 constant values in current climate models, in particular for those models that started to incorporate the

126 representation of dust mineralogy into their schemes (Scanza et al., 2015; Perlwitz et al., 2015a,

127 2015b).

128 Improving our knowledge of the spectral SW refractive index of mineral dust and its relation to particle

129 composition (henceforthand origin) is also key for the detection of dust aerosols in the atmosphere and

130 the quantification of its mass loading, and total andor absorption spectral optical depth from active and

131 passive remote sensing (e.g., Ridley et al., 2016). As an example, the retrieval of the dust SSA and

132 optical depth over bright desert surfaces with the MODIS (Moderate Imaging Resolution Spectroradi-

133 ometer) Deep Blue algorithm (Hsu et al., 2004) applies the Critical Surface Reflectance Method (Kauf-

134 man, 1987) to retrieve dust properties from measured Top of Atmosphere (TOA) spectral reflectance.

135 This algorithm depends critically on a priori information on the spectral refractive index (Kaufman et al.,

136 2001; Yoshida et al., 2013). Similarly, active remote sensing techniques (lidar, light detection and rang-

137 ing) require the knowledge of the extinction- to- backscatter ratio (the lidar ratio), which is also a strong

138 function of the complex index of refraction or SSA of the aerosol particles (e.g., Gasteiger et al., 2011;

139 Shin et al., 2018). Gasteiger et al. (2011) have shown in fact that a 5% change in the SSA at 532 nm

140 can modify by up to 20% the lidar ratio of dust, which means a 20% change in the estimated profile of

141 the dust extinction coefficient and retrieved optical depth from lidar measurements.

142 In this paper we address these issues by reporting the results of a new laboratory investigation of the

143 shortwave refractive index and SSA of dust from various source regions worldwide, in the framework

144 of the RED–DUST project (Di Biagio et al., 2017a; hereafter DB17; Caponi et al., 2017; hereafter C17).

145 Dust optical properties at discrete wavelengths between 370 and 950 nm are derived in conjunction

146 with the particle elemental and mineralogical composition, including total elemental iron and iron oxides.

147 We investigate the relationship of k and SSA to the iron content to provide a parameterization of the

148 dust absorption as a function of its mineralogy, which can be applied to climate models. The depend-

149 ence of dust absorption on the particle coarse size fraction is also investigated to evaluate the change

150 of dust absorption with atmospheric transport time.

151

2. Experimental set–up and instrumentation

153 As previously described in DB17 and C17, aAll experiments discussed here and previously described

154 in DB17 and C17 were conducted in the 4.2 m^3 stainless–steel CESAM chamber (French acronym for

155 Experimental Multiphasic Atmospheric Simulation Chamber) (Wang et al., 2011). Mineral dust aerosols

156 were generated by mechanical shaking of parent soils using about 15 g of soil sample (first sieved to

157 <1000 μm and then dried at 100 °C) placed in a 1 L Büchner flask and shaken for about 30 min at 100

158 Hz by means of a sieve shaker (Retsch AS200). The dust suspension in the flask was injected into the

159 chamber by flushing with N$_2$ at 10 L min^{-1} for about 10–15 min. After injection in the chamber, the largest

160 fraction of the dust aerosol (>1.5 μm diameter) remained in suspension for approximately 60 to 120 min

161 thanks to a four–blade stainless steel fan located at the bottom of the chamber, which also ensured

162 homogeneous conditions within the chamber volume. The submicron dust fraction, instead, remained

163 constant with time during the experiments (see Sect. 4.1.1)~~, as shown in Fig. 3 reporting the timeline of~~

164 ~~the measured effective dust fine diameter~~. The evolution of the physico–chemical and optical properties

165 of the suspended dust was measured by different instruments connected to the chamber. The spectral

166 particle volume dry scattering (β_{sca}) and absorption (β_{abs}) coefficients were measured, respectively, by

167 a 3–wavelength nephelometer (TSI Inc. model 3563, operating at 450, 550, and 700 nm; 2 L min^{-1} flow

168 rate, 2–s time resolution) and a 7–wavelength aethalometer (Magee Sci. model AE31, operating at 370,

169 470, 520, 590, 660, 880 and 950 nm; 2 L min^{-1} flow rate, 2–min time resolution). The size distribution

170 of aerosols was measured by means of a scanning mobility particle sizer (SMPS, TSI, DMA Model

171 3080, CPC Model 3772; mobility diameter range 0.019–0.882 µm; 2.0/0.2 L min^{-1} sheath–aerosol flow

172 rates, 135–s time resolution), a WELAS optical particle counter (OPC) (PALAS, model 2000, white light

173 source between 0.35 and 0.70 µm; optical–equivalent diameter range 0.58–40.7 µm; 2 L min^{-1} flow

174 rate, 1–min time resolution) and a SkyGrimm OPC (Grimm Inc., model 1.129, 0.655 µm operating wave-

175 length; optical–equivalent diameter range 0.25–32 µm; 1.2 L min^{-1} flow rate, 6–s time resolution). Aer-

176 osol elemental and mineralogical composition, including iron oxides, was derived by analysis of dust

177 samples collected on polycarbonate filters (47–mm diameter Nuclepore, Whatman, nominal pore size

178 0.4 µm) mounted ~~i~~on a custom–made stainless–steel sample holder (operated at 6 L min^{-1}) for most of

179 the duration of each experiment.

180 All instruments (size, SW optics, filters) sampled air from the chamber. To equalize the airflow extracted

181 by the different instruments, a particle–free N_2/O_2 mixture airflow was continuously injected into the

182 chamber. Inlets for all extractive measurements consisted of a stainless steel tube located inside

183 CESAM, and an external connection of silicone tubing (TSI Inc.) from the chamber to the instruments,

184 for a total length varying between 0.4 and 1.2 m. As detailed in DB17 and shown in Fig. S1 in the

185 supplement, the transmission efficiency due to aspiration and transmission in the sampling lines as a

186 function of particle diameter was estimated to calculate the effective dust fraction sensed by each in-

187 strument, taking into account the sampling flow rate, tubing diameter, tubing geometry, and particle

188 shape and density. For the nephelometer and the aethalometer, the length of the sampling line from

189 the intake point in the chamber to the instrument entrance was about 1.2 m, which resulted in a 50%

190 cutoff of the transmission efficiency at 3.9 µm particle geometric diameter and 100% cutoff at 10 µm.

191 For the filter sampling system, the length of the sampling line of about 0.5 m resulted in a 50% (100%)

192 cutoff at 6.5 µm (15 µm) particle geometric diameter (or 50% cutoff at 10.6 µm aerodynamic diameter

193 as indicated in C17, therefore compositional analyses refer to the $PM_{10.6}$ size fraction). For the WELAS,

194 the only OPC considered for size distribution in the coarse fraction (see Sect. 2.2), the 50% (100%)

195 cutoff was reached for particles of 5 µm (8 µm) diameter.

196 All experiments were conducted at ambient temperature and relative humidity <2%. In addition to over-

197 night evacuation, the chamber was manually cleaned between experiments to avoid contaminations

198 from remaining dust. Background concentrations of aerosols in the chamber were less than 2.0 µg m^{-3}

199 (that is 10^2 to 10^5 times smaller~~less~~ than the concentration of dust aerosols in suspension in the cham-

200 ber during experiments)

201 A flowchart of the procedure used to treat and combine optical, size, and compositional data, and the
202 algorithm for SSA and complex refractive index retrieval is shown in Fig. 1. Full details of data treatment
203 for size distribution measurements and filter compositional data are provided in DB17 and C17, and in
204 the following we only mention the main points of interest for the present paper. Full details on the data
205 treatment of the SW optical data are provided in Sect. 2.1 and 3.

206 The optical and size datasets were acquired at different temporal resolutions and then averaged over
207 compatible 10–min intervals, whereas the compositional data represent the experiment integral. The
208 SSA and complex refractive index data were retrieved both at 10–min resolution and as experiment
209 averages to relate them to both size and compositional data. Table 1 summarizes the uncertainties on
210 the measured and derived parameters described in the following.

211 **2.1 SW optical measurements**

212 **2.1.1 Aerosol scattering coefficient**

213 The aerosol scattering coefficients (β_{sca}) at 450, 550, and 700 nm are measured by the nephelometer
214 at angles between 7° and 170° and need to be corrected for the restricted field–of–view of the instru-
215 ment (truncation correction) to retrieve β_{sca} at 0°–180°. The truncation correction factor (C_{trunc}), i.e., the
216 ratio of the β_{sca} at 0°–180° and 7°–170°, was estimated by Mie calculations for homogeneous spherical
217 particles using the size distribution measured simultaneously behind SW inlets (see Sect. 2.2). In the
218 calculations, the real part of the complex refractive index of dust was assumed to be wavelength–inde-
219 pendent and fixed at a value of 1.53, while the imaginary part was set to 0.003 at 450 and 550 nm and
220 to 0.001 at 700 nm, according to pre–existing information (Sinyuk et al., 2003; Schladitz et al., 2009;
221 Formenti et al., 2011; Rocha–Lima et al., 2018). For the different dust samples, C_{trunc} ranged between
222 1.2 and 1.7 and decreased with wavelength and the dust residence time in the chamber, following the
223 relative importance of the coarse component in the dust population (Anderson and Ogreen, 1998). The
224 uncertainty on C_{trunc}, calculated by repeating the optical calculations by using the size distribution of
225 dust within its error bars as input to the optical code, is less than ±5% at all wavelengths (in the approx-
226 imation of Mie spherical and homogeneous particles.). In order to assess the consistency of the derived
227 truncation correction, we made a sensitivity study in which we recalculated C_{trunc} by varying the refrac-
228 tive index atused as input to the Mie calculations in the range of n and k values obtained in this study
229 (i.e., values at the 10% and 90% percentile as reported in Table 5 for the whole dataset, that is n
230 between 1.49 and 1.54 and k between 0.001 and 0.006 at 450, 550, and 700 nm). The results of this
231 sensitivity study indicate that, for fixed dust size distribution, the truncation correction C_{trunc} varies less
232 than 1% for n between 1.49 and 1.54, and <5% for k between 0.001 and 0.006, and so that it is quite
233 insensitive to the exact assumed n and k values.

234 Once corrected for truncation, the spectral β_{sca} was extrapolated at the aethalometer wavelengths. With
235 this aim, the Scattering Ångström Exponents, $SAE_{450-550}$ and $SAE_{550-700}$, were calculated as the linear
236 fit of β_{sca} vs λ at 450–550 nm and 550–700 nm, respectively. The $SAE_{450-550}$ and $SAE_{550-700}$ coefficients
237 were used to extrapolate β_{sca} at wavelengths respectively lower and higher than 550 nm. Extrapolated
238 β_{sca} values were used to derive an average SAE of dust for the entire investigated spectral range.

2.1.2 Aerosol absorption coefficient

The aerosol absorption coefficient (β_{abs}) at 370, 470, 520, 590, 660, 880, and 950 nm was retrieved from aethalometer measurements. The aethalometer measures the attenuation (ATT) through an aerosol–laden quartz filter, related to the spectral attenuation coefficient (β_{ATT}) as:

$$\beta_{ATT}(\lambda) = \frac{\Delta ATT(\lambda)}{\Delta t}\frac{A}{V} \quad (1)$$

where A is the area of the aerosol collection spot (0.5 ± 0.1) cm^2 and V the air sample flow rate (0.002 m^3 min^{-1}). The slope $\frac{\Delta ATT(\lambda)}{\Delta t}$ is the linear fit of the measured attenuation as a function of time calculated over 10–min intervals. The spectral attenuation coefficient was converted into an absorption coefficient β_{abs} following the formula by Collaud Coen et al. (2010):

$$\beta_{abs}(\lambda) = \frac{\beta_{ATT}(\lambda)-\alpha(\lambda)\beta_{sca}(\lambda)}{C_{ref}R(\lambda)} \quad (2)$$

The $\alpha(\lambda)\beta_{sca}(\lambda)$ term accounts for the fraction of the measured attenuation due to side and backward scattering and not to light absorption. The Collaud–Coen correction scheme has been recently shown to yield quite accurate values of the absorption coefficients and absorption Ångström exponents from aethalometer data (Saturno et al., 2017). The value of $\alpha(\lambda)$ was calculated with the formula by Arnott et al. (2005) and varied between 0.002 and 0.02 (<±1% from formal error propagation on the Arnott formula), while $\beta_{sca}(\lambda)$ is the scattering coefficient from the nephelometer extrapolated to the aethalometer wavelengths. C_{ref} accounts for multiple scattering by the filter fibers, aerosol laden or not. Its spectral value, obtained by the linear extrapolation of C_{ref} at 450 and 660 nm estimated for mineral dust by Di Biagio et al. (2017b), varied between 4.30 at 370 nm ~~to~~and 3.32 at 950 nm. We assume for the extrapolated C_{ref} an uncertainty of ±10% as estimated in Di Biagio et al. (2017b). The correction factor, R, accounts for the decrease in the aethalometer sensitivity with the increase of the aerosol filter loading. The value of R depends on the absorptivity properties of the sampled aerosol and can be calculated as a function of the particle SSA. In this study, we calculated R by estimating a first–guess SSA* as the ratio of the nephelometer–corrected β_{sca} and β_{ext} obtained as the sum of β_{sca} and the β_{abs} non–corrected for filter loading effect. The R was estimated by using the Collaud–Coen et al. (2010) formulation. For the range of estimated SSA* (about 0.60 to 0.99), R varied between 0.5 and 1.0 (±1–10%).

The Absorption Ångstrom Exponent (AAE) was calculated as the power–law fit of β_{abs} versus λ.

Due to an instrumental problem, aethalometer data were not always available, with a typical 30–min interruption usually 10 to 30 minutes after the beginning of experiments.

2.2 Size distribution

The aerosol number size distribution was obtained from SMPS, WELAS and SkyGrimm measurements over different diameter ranges. The measured electrical mobility and optical equivalent diameters from the SMPS and the OPCs were first converted into geometrical diameters (D_g) as described in DB17 and summarized in Table 1. The OPCs conversion assumes ~~for dust~~ a dust complex refractive index

7

273 that in our study was set in the range 1.47–1.53 for n and 0.001–0.005 for k for both the SkyGrimm and

274 the WELAS (following DB17, for more details see Table 1). After conversion, the estimated D_g range

275 was 0.01–0.50 μm for the SMPS, 0.65–73.0 μm for the WELAS, and 0.29–68.2 μm for the SkyGrimm.

276 Due to a calibration issue, data for the SkyGrimm in the range $D_g > 1$μm were discarded, so that the

277 WELAS is the only instrument considered in the super–micron range. A very low counting efficiency

278 was observed for the WELAS below 1 μm and data in this size range were also discarded.

279

280 The SMPS, WELAS, and SkyGrimm data were combined, as detailed in DB17, to obtain the full size

281 distribution of the dust aerosols suspended in the CESAM chamber, $(dN/dlogD_g)_{CESAM}$, and the size

282 distribution behind SW optical instruments inlets, $(dN/dlogD_g)_{SWoptics}$, after taking into account particle

283 losses along sampling lines (see Supplementary material and Fig. S1). As previously discussed, due

284 to the particle losses in the sampling line from the chamber to the nephelometer/aethalometer, the

285 $(dN/dlogD_g)_{SWoptics}$ size distribution is cut at 10 ~~μm~~microns, so no particles above this diameter reach

286 the SW instruments.

287 The measured size distributions, $(dN/dlogD_g)_{CESAM}$ and $dN/dlogD_g)_{SWoptics}$, were used to estimate the

288 mass concentration of aerosols and their effective diameter (D_{eff}) in the CESAM chamber and behind

289 the SW instrument inlets as:

290
$$\text{Mass concentration} = \int \frac{\pi}{6} D_g^3 \frac{dN}{dlogD_g} \rho \cdot dlogD_g \qquad (3)$$

291
$$D_{eff} = \frac{\int D_g^3 \frac{dN}{dlogD_g} dlogD_g}{\int D_g^2 \frac{dN}{dlogD_g} dlogD_g} \qquad (4)$$

292 The effective dust density ρ in Eq. (3) was set at 2.5 g cm^{-3}, a value that is approximately in the middle

293 of the range of desert dust densities reported in the literature, i.e., 2.1–2.75 g cm^{-3} (Maring et al., 2000;

294 Iwasaka et al., 2003; Reid et al., 2003). The effective diameter was evaluated separately for the fine

295 and coarse fractions of dust by integrating Eq. (4) for diameters ≤1 μm ($D_{eff,fine}$) and >1 μm ($D_{eff,coarse}$),

296 respectively. For $D_{eff,coarse}$ the upper limit of the calculation is 10 μm when calculated from

297 $(dN/dlogD_g)_{SWoptics}$, i.e. measured behind the SW inlets.

298 The dust size distribution, $(dN/dlogD)_{SWoptics}$, measured at each 10–min time step for each sample was

299 fitted with a sum of five lognormal functions to smooth data inhomogeneities linked to the different

300 instrument's operating principles and artefacts. Fitting was performed using the Levenberg–Marquardt

301 algorithm. For each mode, the parameters of the lognormal functions, i.e., the total number concentra-

302 tion (N_i), the geometric median diameter ($D_{g,i}$), and the geometric standard deviation of the distribution

303 (σ_i), were retrieved. The uncertainties in the retrieved parameters were estimated by repeating the fit

304 using size data within their uncertainties. The resulting parameters of the fits at the peak of the injection

305 in the chamber are reported in Table S1, and an example of size fitting is shown in Fig. S2.

306 The procedure described here to estimate $(dN/dlogD_g)_{CESAM}$ and $(dN/dlogD_g)_{SWoptics}$ implies that as-
307 sumptions are made on the values of n and k to correct OPCs data, and this may introduce a circularity
308 in the estimates of the refractive index of dust that use $(dN/dlogD_g)_{SWoptics}$ as input in optical calculations
309 (see Sect. 3.2). In order to analyze the dependence of the results on this assumption, we made a
310 sensitivity calculation by varying the values of n and k used for OPCs corrections within the range of
311 values retrieved in this study (10% and 90% percentiles in Table 5, i.e., 1.49–1.54 for n and 0.001–
312 0.006 for k). We concluded that changing n and k in this range has a very low impact on the retrieved
313 number size distribution behind the SW inlets $(dN/dlogD_g)_{SWoptics}$ compared to the original assumptions
314 made in our calculations (<5% changes in the retrieved size number distribution at the different diame-
315 ters between the original correction and the correction by varying n and k). This is due to the fact that
316 when changing D_g due to changes in the n and k in the OPCs correction, the loss function also modifies
317 to values corresponding to the new D_g. Given that the loss function increases/decreases for increas-
318 ing/decreasing D_g, the combined changes in D_g and the loss function compensate so that the net num-
319 ber concentration behind the SW inlets varies less than a few percent. These results therefore suggest
320 that the procedure to estimate the complex refractive index of dust is nearly independent of the assumed
321 OPC correction.

322 Other sources of uncertainties are linked to the spherical assumption to perform the optical to geomet-
323 rical diameter conversion (discussed in Sect. 3.3) as well as those due to Mie resonance oscillations of
324 the calculated scattering intensities. Concerning Mie resonances, a sensitivity study was performed
325 varying the size resolution of our calculations (high/low diameter resolution in the calculations to have
326 a better/worse reproduction of Mie resonance oscillations) and show that Mie resonances impact the
327 optical to geometrical correction by less than 1%.

328 **2.3 Dust elemental and mineralogical composition and iron content**

329 The elemental and mineralogical composition of the dust aerosols in the $PM_{10.6}$ size fraction was esti-
330 mated by combining different techniques: X–ray diffraction (XRD, Panalytical model Empyrean diffrac-
331 tometer) to estimate the particles' mineralogical composition in terms of clays, quartz, calcite, dolomite,
332 gypsum, and feldspars; wavelength dispersive X–ray fluorescence (WD–XRF, Panalytical PW–2404
333 spectrometer) to determine the dust elemental composition (Na, Mg, Al, Si, P, K, Ca, Ti, Fe); and X–
334 ray absorption near–edge structure (XANES) to retrieve the content of iron oxides and their speciation
335 between hematite and goethite. The dust mass collected on Nuclepore filters during the experiments
336 varied between 0.3 and 6 mg m^{-3} as calculated from elemental concentrations according to Lide (1992).

337 Full details on the XRD, WD–XRF, and XANES measurements and data analysis are provided in DB17
338 and C17. In this study, we discuss the dust elemental iron mass concentration, $MC_{Fe\%}$, i.e., the percent
339 mass of elemental iron with respect to the total dust mass concentration, and the iron oxides mass
340 concentration, $MC_{Fe-ox\%}$, i.e., the percent mass fraction of iron oxides with respect to the total dust mass
341 concentration, estimated as the sum of goethite ($MC_{Goet\%}$) and hematite ($MC_{Hem\%}$) species.

342 **3. Strategy for data analysis**

3.1 Calculation of the spectral extinction coefficient and SSA from scattering and absorption coefficients

The spectral scattering and absorption coefficients, $\beta_{sca}(\lambda)$ and $\beta_{abs}(\lambda)$, measured by the nephelometer and the aethalometer were used to estimate 10–min averages of the spectral extinction coefficient, $\beta_{ext}(\lambda)$, at the 7–λ of the aethalometer between 370 and 950 nm as:

$$\beta_{ext}(\lambda) = \beta_{abs}(\lambda) + \beta_{sca}(\lambda) \qquad (5).$$

The Extinction Ångström Exponent (EAE) was calculated as the power–law fit of β_{ext} versus λ.

The spectral single scattering albedo of dust at 10–min resolution (SSA_{10-min}) was retrieved as:

$$SSA_{10\text{-}min}(\lambda) = \frac{\beta_{sca}(\lambda)}{\beta_{ext}(\lambda)} \qquad (6).$$

The experiment–averaged SSA (λ) was calculated for each soil type based on the following formula (Moosmüller et al., 2012):

$$SSA(\lambda) = \left(1 + \frac{1}{m(\lambda)}\right)^{-1} \qquad (7)$$

where m (λ) represents the slope of the linear fit between the 10–min averages of $\beta_{sca}(\lambda)$ and $\beta_{abs}(\lambda)$ measured along the whole duration of each experiment. An example of $\beta_{sca}(\lambda)$ versus $\beta_{abs}(\lambda)$ fitting to retrieve the spectral SSA is shown in Fig. S3 in the Supplement. The correlation coefficient R^2 of the β_{sca} versus β_{abs} fit usually ranges between 0.97 and 1 at all wavelengths. As will be discussed later in the paper, the single scattering albedo of dust depends on the particle coarse size fraction, and during our experiments SSA_{10-min} was not derived continuously for the different samples due to the aethalometer measurement interruptions. The application of Eq. (7) avoids any bias in the calculated averaged SSA for different soils due to size effects. For two of the analyzed samples (Tunisia and Namib–2), however, the linear fitting procedure was not applicable due to the fact that, respectively, only two and one absorption measurements from the aethalometer were available just after the peak of the injection, with no data afterwards. Average SSA data for Tunisia were thus estimated as the mean of the two available SSA_{10-min} data points, while the single SSA_{10-min} measurement at the peak of the injection was reported for Namib–2. This difference in time sampling should be kept in mind when comparing ~~SSA~~ data for these two samples to the rest of the dataset.

3.2 Retrieval of the spectral complex refractive index

An optical calculation was performed to estimate the complex refractive index (m=n–ik) of dust aerosols based on optical and size data. The retrieval algorithm consisted in recalculating the spectral scattering $\beta_{sca}(\lambda)$ and absorption $\beta_{abs}(\lambda)$ coefficients measured at each 10–min interval by using the fitted $(dN/dlogD)_{SWoptics}$ size distribution as input and by varying the real and imaginary parts of the complex refractive index in the calculations until the best agreement between measurements and calculations was found. At each wavelength the root mean square deviation (RMSD) was calculated as:

$$RMSD(\lambda) = \sqrt{\left[\frac{\beta_{sca,measured}(\lambda) - \beta_{sca,calculated}(\lambda)(n,k)}{\beta_{sca,calculated}(\lambda)(n,k)}\right]^2 + \left[\frac{\beta_{abs,measured}(\lambda) - \beta_{abs,calculated}(\lambda)(n,k)}{\beta_{abs,calculated}(\lambda)(n,k)}\right]^2}$$

(8)

The RMSD was minimized at each wavelength to obtain n–k pairs that most closely reproduce the measured scattering and absorption coefficients. Optical calculations were performed at the 7 wavelengths of the aethalometer between 370 and 950 nm using Mie theory. ~~for homogeneous spherical particles.~~ In the calculations, the real part of the refractive index was varied in the range 1.40–1.60 at steps of 0.01, while the imaginary part was varied in the range 0.0001–0.050 at steps of 0.0001. For each sample, this resulted in 10500 computations per wavelength and per 10–min time step. The uncertainty on the real and imaginary parts of the refractive index was estimated with a sensitivity study. For this purpose, the values of n and k were also obtained by using as input the observed $\beta_{sca}(\lambda)$, $\beta_{abs}(\lambda)$, and $(dN/dlogD)_{SWoptics}$, plus or minus one standard deviation on their measurement. The deviations of the values of n and k retrieved in the sensitivity study with respect to those obtained in the first inversions were assumed to correspond to the one standard deviation uncertainty of 10–min retrieved values.

Experiment–averaged values of the spectral n and k were estimated as the average of single n and k values retrieved at 10–min steps (indicated as n_{10-min} and k_{10-min}). In fact, differently from the SSA, the refractive index did not seem to depend on the particle coarse size fraction (Sect. 4.5).

A control experiment was performed with submicron ammonium sulphate aerosols (see DB17 and supplementary Fig. S4) with the aim of validating the proposed methodology to estimate the aerosol complex refractive index for a non–absorbing aerosol type. For ammonium sulphate particles with a mono–modal size distribution centered at 0.06 µm, as measured with the SMPS, the retrieved real part of the refractive index was 1.56 (±0.01) in the 450–700 nm wavelength range, as expected from literature (Toon et al., 1976; Flores et al., 2009; Denjean et al., 2014).

3.3 Assumptions on the retrieval of SSA and complex refractive index

The approach used to retrieve the SSA and the complex refractive index of dust and the accuracy of the results depend on the accuracy of the input data and the assumptions in the optical calculations. We discuss here two points of the applied procedure, in part already mentioned in the previous paragraphs.

1/ The size distribution from OPCs and also the scattering coefficient from the nephelometer used as input to the n and k retrieval procedure and SSA calculation depend more or less directly on the dust refractive index. These instruments need in fact to be corrected for instrumental artefacts and these corrections require an a priori knowledge of the n and k, which in our approach were set to fixed values (1.47–1.53 for n and 0.001–0.005 for k for OPCs optical to geometrical diameter conversion, and 1.53 for n and 0.001–0.003 for k for nephelometer truncation correction). This choice may in principle introduce a certain degree of uncertainty and circularity into the derived n, k, and SSA for dust. Nonetheless, we note that the range of refractive index values used to correct OPCs and nephelometer data falls in

the range of variability of the refractive index values obtained in this study (see Sect. 4.3), which suggests that the values used for the corrections are appropriate. Additionally, as previously discussed, both the size distribution $(dN/dlogD_g)_{SWoptics}$ and the scattering coefficient are not very sensitive to the assumptions about n and k used for the calculations (less than 5% changes in both the number size distribution behind SW inlets and the scattering coefficient from changing n and k within the range of estimated values in this study) which further demonstrates the robustness of the proposed approach.

2/ The retrieval procedure for n and k, as well as the calculations for OPCs optical–to–geometrical diameter and the nephelometer truncation correction, simplifies the non–spherical heterogeneous dust aerosols (e.g., Chou et al. 2008; Okada et al., 2011; Nousiainen and Kandler, 2015) into homogeneous spherical particles that can be represented by Mie theory. In the present study, we decided not to use a more advanced shape–representing theory for three main reasons. First, the spherical model has been shown to produce only moderate errors when computing angular–integrated quantities (Mishchenko et al., 1995; Otto et al., 2009; Sorribas et al., 2015) such as those we calculate in this study to retrieve the OPC and truncation corrections and for n and k retrieval. For instance, Sorribas et al. (2015) showed that using a spheroidal model has a negligible effect on the truncation correction. These authors estimated that using a spheroidal model permits to improve by 4 to 13% the agreement between modelled and measured spectral scattering coefficient at 450–700 nm but only for supermicron particles. Conversely, for submicron dust the spherical approximation is better suited than the spheroidal model to reproduce the scattering coefficients by the nephelometer. The study by Mogili et al. (2007) also found an excellent agreement between measured shortwave extinction spectra and those calculated from Mie theory simulations for dust minerals, supporting the use of Mie theory for dust optical modelling. On the other side, other studies point to the need of a non–spherical assumption to improve the modelling of dust optical properties (e.g., Otto et al., 2009). Second, we used Mie theory for the sake of comparison with the large majority of previous field and laboratory data published so far, which had used calculations with the spherical approximation Third, given that the shape distribution and morphology of the dust samples was not measured during experiments. I. Improper assumptions on the particle shape and morphology may in fact induce even larger errors than using Mie theory, in particular for super–micron aerosols (Kalashnikova and Sokolik, 2004; Nousiainen and Kandler, 2015). It should be pointed out, however, that dust is usually assumed to be spherical in global climate models (e.g., Myhre and Stordal, 2001; Balkanski et al., 2007; Jin et al., 2016), and different studies still show contrastingdictory results on the true impact of dust non–sphericity on radiative fluxes and heating rates from global model simulations (Mishchenko et al., 1995; Yi et al., 2011; Räisänen et al., 2012; Colarco et al., 2014). On the other hand, shape effects can be important for the retrieval of aerosol properties from remote sensing techniques using spectral, angular, and polarized reflectance measurements (e.g., Feng et al., 2009). In synthesis, accounting for shape effects is still controversial for dust modelling and also a complex issue beyond the scope of this paper. Thus, while we acknowledge the potential uncertainties induced by spherical assumptions in our study, we do not quantify here the overall impact of this assumption on our results.

4. Results

452 Nineteen soil samples from different desert areas in Northern Africa, Sahel, Eastern Africa and the

453 Middle East, Central Asia, Eastern Asia, North America, South America, Southern Africa, and Australia

454 were selected for experiments from a collection of 137 soil samples from source areas worldwide. The

455 main information on the provenance of these soils is provided in Table 2. The nineteen selected soils,

456 the same as analyzed in DB17, represent the major dust source regions depicted in Ginoux et al. (2012).

457 Amongst the database of 137 samples from all the world regions that constitute significant dust emitters,

458 this range in mineralogical composition represents the largest variability in iron oxides contents that can

459 be found worldwide. This is illustrated in Fig. 2 where we represent the variability of hematite and goe-

460 thite content in the nineteen selected soils and compare it with the range of variability of the global

461 desert soils from the database of Journet et al. (2014).

462 **4.1 Physical and chemical properties of analysed dust samples**

463   **4.1.1 Dust mass concentration and size distribution**

464 Figure 3 shows a typical example of a time series of aerosol mass concentration and effective fine and

465 coarse diameters measured inside the CESAM chamber and behind the SW instruments inlets during

466 the experiments, as well as the corresponding β_{sca} and β_{abs} at 370 nm. The Figure shows the rapid

467 increase of the mass concentration within CESAM during dust injection in the chamber, and its subse-

468 quent decrease during the experiments due to both size–selective gravitational settling, occurring

469 mostly within the first 30 min of experiments, and dilution by sampling. The scattering and absorption

470 coefficients of dust decrease with time after injection in tandem with the decrease of the mass concen-

471 tration and the size–dependent depletion in the chamber. The dust mass concentration inside CESAM

472 at the peak of the injection is between 2 mg m^{-3} (Mali) and 310 mg m^{-3} (Bodélé) and falls to values

473 between 0.9 mg m^{-3} (Mali) and 20 mg m^{-3} (Bodélé) behind the SW instruments inlets. These values

474 are comparable to those measured close to sources during dust storms (Rajot et al., 2008; Kander et

475 al., 2009). After ~~a~~ 2 ~~–~~hour~~s experiment~~, the dust mass concentration has decreased to values of 0.2 to

476 2.5 mg m^{-3} (inside CESAM) and of 0.1 to 1.9 mg m^{-3} (behind the SW inlets), ~~within a range of values~~

477 ~~comparable to what has been measured~~as after medium– to long–range dust transport in the real at-

478 mosphere (Weinzerl et al., 2011; Denjean et al., 2016b). Th~~ei~~s~~e data therefore~~ indicate~~s~~ that in a 2–

479 hour experiment in CESAM it is possible to reproduce the temporal changes of the dust mass load

480 observed in the real atmosphere ~~for dust~~ from ~~its~~ emission to medium/long–range transport~~a receptor~~

481 ~~site~~.

482 ~~Concurrently with~~As the mass concentration, the effective diameter of the coarse fraction, $D_{eff,coarse}$, ~~of~~

483 ~~the coarse fraction of the dust aerosol~~ also rapidly decreases with time due the progressive deposition

484 of the coarsest particles in the chamber. For the ~~different analyzed~~various soils, $D_{eff,coarse}$ varies in the

485 range of 4–8 µm (peak of injection) to 3–4 µm (after 2 hours) inside the CESAM chamber, and in the

486 range of 3–4 µm (peak of injection) to 2–3 µm (after 2 hours) behind the SW inlets. In contrast, $D_{eff,fine}$

487 remains quite constant during the experiments, with a value between 0.6 and 0.7 µm for all soils. The

488 values of $D_{eff,coarse}$ obtained in this study inside the CESAM chamber are in line with those measured

489 close to African sources (4–12 µm, Rajot et al., 2008; Weinzerl et al., 2009; Ryder et al., 2013a) and

490 for dust transported across the Mediterranean (5–8 µm, Denjean et al., 2016a). Conversely, the values

491 of $D_{eff,coarse}$ behind the SW instruments inlets are mostly in agreement with those reported for dust trans-

492 ported at Cape Verde and across the Atlantic ocean (~3 μm, Maring et al., 2003; Müller et al., 2011;

493 Denjean et al., 2016b). Our values of $D_{eff,fine}$ are higher compared to values reported by Denjean et al.

494 (2016a) for dust aerosols transported over the Mediterranean (0.2 to 0.5 μm), reflecting the fact that

495 we analyse pure dust whereas these authors often encountered dust externally mixed with pollution

496 particles.

497 The comparison of $D_{eff,coarse}$ values suggests that while the size of dustdistribution in CESAM is mostly

498 representative of dust close to sources, (seeas already pointed out in DB17), the size measured behind

499 the SW instruments inlets is mostly representative of transport conditions. Figure 4 illustrates this point

500 by showing the volume size distributions of the generated dust aerosols at the peak of injection seen

501 by the SW optical instruments, compared to the average size of dust measured in CESAM (DB17) and

502 field observations close to sources (e.g., Niger) and after long–range transport (Cape Verde, Suriname,

503 and Puerto Rico, and Barbados). The size distribution of dust inside CESAM includes a coarse mode

504 up to ~ 50 μm tenths of micrometres and well reproduces field observations close to sources, as shown

505 in comparison to the Niger case. Due to particle losses along tubes, the coarsest particles above 10 μm

506 diameter are not seen by the SW instruments. The overall shape of the dust size distribution sensed by

507 the SW instruments is comparable to that measured during after atmospheric long–range transport,

508 even if the fraction of particles above 3.9 10 μm diameterdiameter, which is at the 50% cutoff of the

509 transmission efficiency for the SW optical instruments, is significantly under–represented compared to

510 observations. (i.e., Betzer et al., 1988; Formenti et al., 2001; Maring et al., 2003; Ryder et al., 2013b,

511 2018; Jeong et al., 2014; Denjean et al., 2016b). It should be keep in mind that often also field data are

512 affected by inlet restrictions so that they cannot measure the whole coarse dust fraction (see Table 1 in

513 Ryder et al., 2018). The lowest cutoff for field data shown in Fig. 4 are for the NAMMA and PRIDE

514 datasets and correspond to upper size limits at 5 and 10 μm in diameter, respectively. Being these

515 values above our cutoff of 3.9 μm, it means that the comparison with our size dataset is meaningful

516 within the range of our measurements. To note that only the data from AER–D did not suffer from

517 significant inlet restrictions thus leading to the observation of giant dust particles up to tens of microns

518 in the Saharan Air Layer off the coasts of Western Africa.

519 **4.1.2 Iron and iron oxide dust content**

520 Elemental iron includes the iron in the form of iron oxides and hydroxides, i.e. hematite and goethite

521 (the so–called free iron, mostly controlling SW absorption) and the iron incorporated in the crystal struc-

522 ture of silicates and alluminosilicates (illite, smectite), which does not substantially contribute to SW

523 absorption (Karickhoff and Bailey, 1973; Lafon et al., 2004). The mass concentrations of these compo-

524 nents (total iron oxides, hematite, goethite, and total elemental iron) for the different analysed samples

525 are reported in Table 3. TThere is a considerable variability in the iron and iron oxide content for our

526 samples. Total iron in the dust samples is in the range from 2.4% (Namib–1) to 10.6% (AustraliaNamib–

527 2). Iron oxides account for 11% and to 62% of the iron mass (calculated following C17, not reported in

528 Table 3), whereas the percent of iron oxides to the total dust mass varies between 0.7% (Bodélé De-

529 pression) and 5.8% (Niger). These data are in the range of values reported in the literature (Reid et al.,

530 2003; Scheuvens et al., 2013; Formenti et al., 2011, 2014a). For the samples from the Sahara and the

531 Sahel, goethite is the dominant iron oxide species, in agreement with Lafon et al. (2006) and Formenti

532 et al. (2014a; 2014b). ~~In contrast, over other regions~~Elsewhere, hematite dominates over goethite, as

533 ~~already~~ reported by some studies (Arimoto et al., 2002; Shen et al., 2006; Lu et al., 2011).

4.2 Spectral– and time–dependent dust extinction and absorption coefficients, complex refrac-

tive index, and SSA

536 Figure 5 illustrates a typical spectral– and time–dependent set of measured optical properties. The

537 spectral extinction coefficient, absorption coefficient, SSA, and real and imaginary parts of the complex

538 refractive index obtained at 10–min resolution for the Morocco and Algeria samples are shown at the

539 peak of the dust injection in CESAM and 30 and 90 min after the peak. Figure 5 shows that absorption

540 decreases with wavelength, but not extinction. The SSA increases from 370 to 590 nm while it is~~shows~~

541 almost constant ~~values~~ between 590 and 950 nm. The imaginary part of the refractive index decreases

542 with λ following the decrease of β_{abs}. The real part of the refractive index does not depend on ~~is almost~~

543 ~~constant with~~ wavelength.

544 The extinction and absorption coefficients decrease in absolute value with time, as already shown in

545 Fig. 3.~~, but t~~Their spectral dependence remains quite constant with time, ~~even if it~~but varies from soil to

546 soil. The experiment–averaged aA~~bsorption, s~~Scattering, and eE~~xtinction Ångström e~~Exponents in the

547 370–950 nm spectral range, representing the spectral variation of the absorption, scattering and extinc-

548 tion coefficients, vary between the values of 1.5 and 2.4 (AAE), –0.4 and 0.4 (SAE), and –0.2 and +0.5

549 (EAE) for the different samples. These values are in line with those previously reported by Moosmüller

550 et al. (2012) and C17 for dust from various locations. The retrieved n and k also show negligible changes

551 of their spectral shape with time and their magnitude remains approximately constant. In contrast, the

552 SSA increases with time, in particular below 600 nm wavelength, and ~~so~~ its spectral shape changes.

553 This is mostly due to the decrease of the coarse size fraction with residence time in the chamber, as

554 will be analysed in Sect. 4.5. Similarly to the absorption, scattering, and extinction coefficients, the

555 spectral shape of k and SSA is somewhat different between the various samples, with the sharpest

556 spectral variations observed for the most absorbing samples and a less pronounced spectral variation

557 for the less absorbing ones, as evident, for example, by comparing the SSA data for Morocco and

558 Algeria in Fig. 5.

4.3 Spectral complex refractive index and SSA for the different source regions and comparison

to literature data

561 Figures 6 and 7 shows the experiment–averaged n, k, and SSA between 370 and 950 nm for the nine-

562 teen aerosol samples analyzed in this study. Data of n, k, and SSA and their uncertainties ~~for each~~

563 ~~sample~~ are reported in Tables 4 and 5 for each sample together with the average values for each of the

564 eight different source regions and for the full dataset. Figures 6 and 7 shows that there are significant

565 differences, both in magnitude and spectral shape, between the imaginary refractive index and SSA for

566 the different samples. The highest values of k (0.0048–0.0088 at 370 nm and 0.0012–0.0021 at 950

567 nm) ~~(~~and lowest values of SSA~~)~~ (0.70–0.75 at 370 nm and 0.95–0.97 at 950 nm) are obtained for the

568 Niger, Mali, Namib–2 and Australia samples, which also show the highest values of both the iron oxide

content between 3.6% and 5.8% and hematite content between 2.0% and 4.8% ~~(k is in the range 0.0048–0.0088 at 370 nm and 0.0012–0.0021 at 950 nm, and SSA is in the range 0.70–0.75 at 370 nm and 0.95–0.97 at 950 nm)~~. The lowest values (k is 0.001 at 370 and 0.0003 at 950 nm, and SSA is in the range 0.91–0.96 at 370 nm and 0.97–0.99 at 950 nm) are obtained for the Bodélé, Namib–1, and Arizona samples, which have iron oxide contents between 0.7% and 1.5% ~~(k is 0.001 at 370 and 0.0003 at 950 nm, and SSA is in the range 0.91–0.96 at 370 nm and 0.97–0.99 at 950 nm)~~. Both k and SSA vary from region to region, with the largest absorptions (highest k, lowest SSA) for the Sahel and Australia and the lowest absorption (lowest k, highest SSA) in North and South America and the Middle East; k and SSA values also vary within the same region, as illustrated ~~in Fig. 6~~ for the Sahelian and Southern African samples. The real part of the refractive index, on the other hand, is not only almost wavelength–independent, as anticipated, but also relatively invariant from sample to sample. Its average over the 370–950 nm spectral range is between 1.48 (Gobi) and 1.55 (Ethiopia and Namib–2).

The full envelope of n, k, and SSA obtained for the entire set of analysed samples is shown in Fig. 8~~7a and 7b (left panels)~~. The real refractive index is relatively invariant, while the spectral k varies by up to an order of magnitude (0.001–0.009 at 370 nm and 0.0003–0.002 at 950 nm). The SSA changes accordingly for the different dust samples at the different wavelengths (30% change at 370 nm corresponding to values between 0.70–0.96 and 4% change at 950 nm for values within 0.95–0.99). The population mean is 1.52 for n (as spectral average) and varies in the range 0.0033–0.0009 for k and 0.85–0.98 for the SSA between 370 and 950 nm (0.0016 and 0.94 as spectral averages for k and SSA) (Fig. 8~~7~~ and Tables 4 and 5).

The comparison between the full envelope of n, k, and SSA in this study with literature data is also shown in Fig. 8~~7a and 7b (right panels)~~. Literature values considered for comparison include estimates from ground–based, aircraft, and satellite observations, laboratory studies, AERONET inversions, and estimates from mixing rules based on the dust mineralogical composition. Given that the sample selection in our experiments fully envelopes the global variability of mineralogy of natural dust, we could expect that our dataset would also fully envelope the global-–scale variability of the dust absorption and scattering properties in the SW. When comparing with available literature data we found that our n and SSA datasets very well ~~envelope~~ encompass the range of values indicated in the literature, with only a few outlier points. In contrast, for the imaginary refractive index the reported range of variability from the literature is significantly larger than that found in our study, with our range of k being mostly at the lower bound of previous results. Nonetheless, our range of k values fully envelopes the ensemble of remote sensing and field campaign data on airborne dust from the previous literature reported in Fig. 7~~8~~a. The global average spectral values for k in our study (thick black line) perfectly match the Dubovik et al. (2002) dataset from a synthesis of AERONET observations from various locations worldwide. Likewise, our k average is also very close to the dataset by Balkanski et al. (2007), estimated from mineralogical composition assuming 1.5% (by~~in~~ volume) of hematite in dust ~~(a value similar to our population average of 1.8% (in mass) for the dust hematite content)~~, a value shown to allow a reconciliation of climate modelling and satellite observations of the dust direct SW radiative effect. By comparison, the average dust hematite content for the ensemble of our analysed samples is 1.8% (in mass), close to the 1.5% value proposed by Balkanski et al. (2007).

609 Looking at Fig. 8~~7~~a, the datasets ~~which~~ that show the largest values, which also fall outside~~deviations~~

610 ~~from~~ our estimated range of k over the entire considered wavelength range are the ones by: (i) Volz

611 (1972), Patterson et al. (1977) and Hess et al. (1998; i.e., the OPAC 3.1 version database, which is the

612 same k dataset used in the new OPAC 4.0 version, Koepke et al., 2015) showing larger values than

613 our dataset over the entire considered wavelength range. These datasets, ~~which~~ are ~~also~~ amongst the

614 most commonly used references for the dust imaginary refractive index in many climate models; and

615 (ii) the dataset by Wagner et al. (2012)~~,~~ obtained from laboratory chamber experiments, deviating es-

616 pecially below 600 nm wavelength from our range of k. ~~from laboratory chamber experiments; and (iii)~~

617 ~~the dataset by Steigmann and Yang (2017), estimated from a machine learning technique.~~ The reasons

618 for these discrepancies in the k values are difficult to assess, since they c~~a~~ould~~n~~ be related to both

619 instrumental and analytical aspects. In the studies by Volz (1972) and Patterson et al. (1977), for in-

620 stance, the complex refractive index was obtained by transmittance and diffuse reflectance on pellet

621 samples, a technique that requires the dust to be pressed in a matrix of non–absorbing material. In this

622 case a discrepancy arises from the different optical behaviour between dust compressed in a pellet and

623 the airborne particles. Moreover, Volz (1972) and Patterson et al. (1977) analyse dust aerosols collected

624 after mid– to long–range transport, thus~~so~~ after the dust ha~~ve been~~s possibly been mixed with absorb-

625 ing species.

626 For the case of Wagner et al. (2012) the imaginary refractive index was retrieved from~~,~~ laboratory

627 chamber experiments on suspended dust, as in our study. Nonetheless, their approach differs in various

628 aspects from the one applied here and this can lead to the observed differences in the retrieved k. First,

629 the aerosol generation technique is different between the two works and this possibly leads to particles

630 with different physico–chemical features compared to our study. In Wagner et al. (2012) the dust aerosol

631 was generated by a rotating brush disperser using only the 20–75 µm sieved fraction of the soils. This

632 system acts to disaggregate the finest particles of the soil by passing it through a nozzle. Then the

633 largest aerosol grains were removed by a cyclone system (50% cutoff at 1.2 µm aerodynamic diameter),

634 so that only the submicron size fraction was measured. We show in Sect. 4.5 that k is independent of

635 size for the range of investigated effective coarse diameters between 2 and 4 µm, but the range of sizes

636 analysed in Wagner et al. (2012) is significantly lower than in our study and a size–effect cannot be

637 excluded. In fact, the relationship between dust absorption and iron content may vary depending on the

638 considered size fraction (see C17) due to the fact that iron bearing minerals are more concentrated in

639 the clay fraction (<2.0 µm) of the dust (Kandler et al., 2009). Moreover, generating dust in a different

640 way may lead to differences in the chemical and mineralogical size–dependent composition of the sam-

641 ple, therefore contributing to the observed differences. The impact of this is however difficult to evaluate.

642 Another difference concerns the choice of the optical theory to retrieve k (T–matrix in Wagner et al.

643 instead of Mie theory as used in our work). This can contribute to the observed differences, even if in a

644 limited way (Mogili et al., 2007; Sorribas et al., 2015). Third, in their retrieval Wagner et al. fixed the real

645 refractive index to a wavelength–independent value of 1.53 (as done in several other field and labora-

646 tory studies in Fig. 8) and this assumption can bias high/low the retrieved k if the actual n is higher/lower

647 than the assumed 1.53 value. So, in summary, while multiple factors could contribute to the discrepancy

648 it remains however difficult to assess which source of discrepancy is dominant.

649

4.4 Imaginary refractive index and SSA versus iron and iron oxide content

The sample–to–sample variability of the imaginary part of the refractive index k and the SSA observed in Fig. 6 and 7 is related to the dust composition by investigating the dependence on the particle iron content. In Fig. 89 we show the experiment–averaged k and SSA at 370, 520, and 950 nm versus the mass concentration of iron oxides (hematite+goethite, $MC_{Fe-ox\%}$), hematite ($MC_{Hem\%}$), goethite ($MC_{Goeth\%}$), and total elemental iron ($MC_{Fe\%}$) measured for the different dust samples analyzed in this study. The data are linearly fitted to relate k and SSA to $MC_{Fe-ox\%}$, $MC_{Hem\%}$, $MC_{Goeth\%}$, and $MC_{Fe\%}$. The results of the fits at all wavelengths between 370 and 950 nm are reported in Table 6, together with the statistical indicators of the goodness of fit (correlation coefficient, R^2, and reduced chi square, χ^2_{red}, i.e., the obtained chi square divided by the number of degrees of freedom). The data in Fig. 8 and Table 6 indicate that there is an excellent correlation between both k and SSA and $MC_{Fe-ox\%}$ at the different wavelengths ($R^2>0.75$). A weaker correlation is found when relating k and SSA to $MC_{Hem\%}$ and $MC_{Fe\%}$ (R^2 between 0.40 and 0.74 for k and between 0.49 and 0.78 for the SSA), and $MC_{Goeth\%}$ (R^2 between 0.17 and 0.62). The better correlation of k and SSA to $MC_{Fe-ox\%}$ compared to $MC_{Fe\%}$ is expected since dust optical properties in the visible wavelengths are mostly sensitive to the fraction of iron oxides, rather than to iron incorporated into the crystal structure of silicates (i.e., Karickhoff and Bailey, 1973; Lafon et al., 2006; Moosmüller et al., 2012; Klaver et al., 2011; Engelbrecht et al., 2016; C17). The quantities that most robustly satisfy a linear relationship are k and $MC_{Fe-ox\%}$, as indicated by the reduced chi square χ^2_{red} that is around 1 at all different wavelengths. The χ^2_{red} increases to values also larger than 2 in the other cases, indicating the poorer robustness of the fit in these cases.

We also investigated the dependence of the spectral k and SSA on the mass concentration of other minerals contained in dust, such as clays, calcite, quartz, and feldspars, and also on the mass concentration of different elements. We found that there is no statistically significant correlation between k and or SSA and the mass concentration of any of these compounds (not shown), with R^2 values between 0.002 and 0.46 at the different wavelengths for all cases.

These results therefore clearly show that iron, particularly in the form of iron oxides (hematite + goethite), is the main driver of dust shortwave absorption. Measuring only the hematite mass fraction to estimate the dust absorption, as it is sometimes done, is therefore not sufficient.

4.5 Imaginary refractive index and SSA versus dust coarse size fraction

The dependence of the spectral k and SSA on the dust coarse fraction is investigated by relating it to the $D_{eff,coarse}$ calculated from the size distribution data behind the SW instruments inlets. The k_{10-min} and SSA_{10-min} at 370, 520, and 950 nm versus $D_{eff,coarse}$ are shown in Fig. 109 for all experimental data, which we separated into three classes based on their iron oxide content ($MC_{Fe-ox\%} \leq 1.5\%$, $1.5\% < MC_{Fe-ox\%} < 3\%$, $MC_{Fe-ox\%} \geq 3\%$). Figure 109 shows that even if the correlation is not very strong ($R^2<0.54$), there is a clearly decreasing tendency for the SSA_{10-min} with increasing $D_{eff,coarse}$, particularly at 370 and 520 nm for strongly absorbing samples with iron oxide content larger than 3%. The SSA_{10-}

686 $_{min}$ is mostly independent of changes of $D_{eff,coarse}$ at 950 nm. Conversely, k_{10-min} has a very poor corre-

687 lation with $D_{eff,coarse}$ ($R^2 < 0.35$) and thus does not depend on size. Similar results were also obtained for

688 the real part (not shown).

689

690 These results confirm previous observations (Sokolik and Toon, 1999; McConnell et al., 2008, 2010;

691 Kandler et al., 2011; Ryder et al., 2013a; 2013b) that the refractive index, an intrinsic property of matter,

692 is independent of size. This suggests that size–dependent mineralogical composition is not sufficient to

693 affect k (in the limit of our measurement and retrieval procedure precision). It is worth mentioning that

694 only few past studies evidenced a dependence of k on the size distribution of the dust aerosols (i.e.,

695 Kandler et al., 2009, 2011; Otto et al., 2009) maybe because the refractive index was retrieved in these

696 studies from mixing rules based on the estimated size–dependent mineralogical composition.,

697 while Differently from k, the SSA increases as the coarse dust size fraction decreases. This is due to

698 the fact that absorption efficiency for a single particle (Q_{abs}) increases with particle diameter while the

699 scattering efficiency (Q_{sca}) decreases. Ryder et al. (2013a) also showed that the dependence of SSA

700 on size is linear, but important only when the coarse fraction is high (if particles larger than about 3 μm

701 in diameter are present), otherwise the SSA depends mainly on composition, also in agreement with

702 more recent field observations by Ryder et al. (2018).

703 **5. Summary and concluding remarks**

704 In this paper we presented new measurements of the spectral SW complex refractive index ($m=n-ik$)

705 and single scattering albedo (SSA) for nineteen mineral dust aerosols generated in the laboratory from

706 natural soil samples from major desert dust source areas in northern Africa, the Sahel, Middle East,

707 eastern Asia, North and South America, southern Africa, and Australia, and selected to represent the

708 heterogeneity of the dust composition at the global scale, in particular the range of iron oxide concen-

709 trations. The envelope of refractive indices and SSA data obtained in this study can thus be taken as

710 representative of the variability of the global dust aerosol.

711 Experiments described here were conducted in the 4.2 m^3 CESAM chamber, a realistic and dynamic

712 environment where dust aerosols can beare generated and maintained in suspension for few several

713 hours while monitoring the evolution of their physical, chemical, and optical properties. The generated

714 dust aerosols are characterized by a realistic size distribution, including both the sub–micron and the

715 super–micron fraction, and they have an atmospherically representative mass concentration and com-

716 position, including iron oxides and elemental iron content.

717 Some other laboratory studies have been performed in the past to investigate the shortwave SSA of

718 dust from different sources worldwide and its dependence on composition (Linke et al., 2006; Moosmül-

719 ler et al., 2012; Engelbrecht et al., 2016). Conversely, for the refractive index there exists to our

720 knowledge only one other chamber study (Wagner et al., 2012), that retrieved the imaginary part k

721 between 305 and 955 nm for dust aerosols from a limited number of source areas in Africa (Burkina

722 Faso, Egypt and Morocco). As a matter of fact, our work provides the first consistent simulation chamber

723 study of the complex refractive index of global dust.

The results of the present study can be summarized as follows:

1. The spectral k and SSA retrieved in this study vary from sample to sample within the same region but also from a region to another. For k, values vary between 0.001~~1~~–0.009~~88~~ at 370 nm, 0.0006 to 0.0048 at 520 nm, and 0.0003–0.002 at 950 nm. For SSA, values vary from 0.70 to 0.96 at 370 nm, 0.85 to 0.98 at 520 nm, and from 0.95 at 0.99 at 950 nm. In contrast, n is wavelength–independent and almost uniform for the different sources, with values between 1.48 and 1.55. Values for n and SSA fall within the range of published literature estimates, while for k we obtain a much narrower range of variability than the ensemble of literature results, as illustrated in Fig. 8~~7~~. In particular, we found lower values of k compared to most of the literature values currently used in climate models, such as Volz et al. (1972), Patterson et al. (1977), and the OPAC database (Hess et al., 1998; Koepke et al., 2015). In their study, Miller et al. (2014) state that the values of Dubovik et al. (2002) from AERONET, Patterson et al. (1977) for far–travelled dust, and OPAC probably bracket the global solar absorption by dust. In contrast, our results indicate that dust absorption is lower than previously thought, and its average is close to the values reported by Dubovik et al. (2002) from AERONET observations and Balkanski et al. (2007) for a dust with a 1.5% volume fraction of hematite. Our range of variability of an order of magnitude for k and between 4% and 30% for the spectral SSA is actually large enough to change the sign of the global dust direct effect at the TOA (Miller et al., 2004), as well as its regional implications (e.g., Solmon et al., 2008; Jin et al., 2016), and has to be taken into account in climate modelling.

2. The documented changes in k and SSA also impact remote sensing retrievals. To give an example, following Gasteiger et al. (2011), our observed variability of about 10% for the SSA at 532 nm would translate to about 40% variability in the retrieved extinction profiles and optical depths from lidar observations for dust from varying sources.

3. The sample–to–sample variability observed in this study is mostly related to the iron oxide and elemental iron content in dust. At each investigated wavelength the magnitude of k and SSA is linearly correlated to the mass concentration of total iron oxides, hematite, goethite, and total elemental iron. Small variations of these compounds translate into large variations of k and SSA. ~~This suggests that it is sufficient to know the content of iron oxide or elemental iron in dust to predict its spectral k and SSA, which represents a huge simplification for parameterizing their regional and global variability.~~

4. We also investigated the dependence of k and SSA on the size distribution of dust. While k is independent of size (suggesting that a constant value can be used along transport), below 600 nm the SSA linearly decreases for increasing $D_{eff,coarse}$ for strongly absorbing samples with more than 3% iron oxide content. T~~T~~he investigated range of $D_{eff,coarse}$ is within about 2 and~~and~~ 4 μm, and thus comparable to values obtained along a transport path over the Atlantic Ocean for dust during about 2 to 6 days following emission (Denjean et al., 2016a).

5. The observations of points 3 and 4 suggest that while it is sufficient to know the content of iron oxide (or elemental iron) in dust to predict its spectral k, which means that only one tracer is needed in models to parametrize its regional and global variability, for the spectral SSA both composition and size distribution are required.

6. Concluding remarks

Based on our results, we recommend that dust simulations, as well as remote sensing retrievals, use source–dependent values of the spectral SW refractive index and SSA instead of generic values. We propose, as a first step, a set of regionally–averaged n, k, and SSA values to represent dust from each of the eight regions analysed here as well as a global average value from the ensemble of our data (Tables 4 and 5). Furthermore, the relationships found between k and SSA and the iron oxides or elemental iron content in dust open the perspective to establish predictive rules to estimate the spectrally–resolved SW absorption of dust based on composition. We recommend the use of iron oxide content rather than iron content as it is better correlated with k and SSA. The relationship found in this study, nonetheless, refer to the bulk composition of the dust aerosols and to a size range typical of 2 to 6 days of transport in the atmosphere. As demonstrated in C17 with for the mass extinction efficiency, the relationships linking the dust absorption to iron content vary as a function of the analysed size fraction due to the fact that iron bearing minerals are more concentrated in the clay fraction (<2.0 µm) than in the coarsest fraction of the dust (Kandler et al., 2009; C17). Further investigation should be therefore addressed to evaluate the dependence of the spectral k and SSA versus iron content as a function of the size distribution of the particles, in particular extending to a wider range of $D_{eff,coarse}$ compared to the one investigated in the present study. This will allow to determine if the k and SSA versus iron relationships change or not in different phases of the aerosol lifetime, so if it is valid close-from the to source areas (when the coarsest fraction is dominant, i.e. $D_{eff,coarse}$ up to 15 µm, Ryder et al. (2013b)), and in to long–range transport conditions (when most of the coarse particle fraction above few µm has settled out (i.e., $D_{eff,coarse}$ of 2–3 µm or lower, Denjean et al. (2016b)).

We point out, however, that the use of mineralogy to estimate k and SSA based on linear relationships, as obtained in our study, requires nonetheless that the model–predicted dust composition accurately reflects that of the natural atmospheric aerosols. To this aim, realistic soil mineralogy databases and accurate modelling of the soil to aerosol size fractionation need to be developed in model schemes. In this sense we mention the EMIT project (Earth Surface Mineral Dust Source Investigation) as a potential near–future source of high resolution surface mineralogy data for arid and semi–arid regions based on imaging spectroscopy satellite data (Green et al., 2018). Also, a realistic representation of the size distribution, in particular the coarse mode fraction of dust and its retention during atmospheric transport, should be provided in models given its importance in affecting the SSA, as shown in this study and previously reported in other papers (Ryder et al., 2013a, 2013b, 2018; Kok et al., 2017).

Our study focuses on the dust spectral optical properties between 370 and 950 nm. Further work is required to extend the range of spectral refractive index and SSA data to wavelengths lower than 370

801 nm or higher than 950 nm given that these data are often required in Global Circulation Models and
802 Numerical Weather Prediction models.

803 We do not provide any quantification of the uncertainty associated with the assumption of spherical
804 particles in our study, even if we acknowledge the potential role of non–sphericity in affecting our data
805 treatment and results. Additional work is foreseen to better investigate the shape of our generated dust
806 and the impact of non–sphericity on retrieved spectral refractive indices and SSA.

807

808 Finally, this study had the objective to investigate the variability of the dust SW optical properties at the
809 global scale in linked to the global variability of the dust composition. It is noteworthy that observations
810 over Southern Africa and the Sahel from the present study indicate that the k and SSA variabilitiesvar-
811 iability over these regions are is comparable to the ones obtained for the global scale. For other regions,
812 such as North America and Australia, only one sample was analyzed, with no information on the re-
813 gional–-scale variability of k and SSA. Additionally, for some of the analyzed areas, such as the Bodélé
814 depression, even local scale variability (on the order of few km) may be of relevance, given the docu-
815 mented local scale changes of the particles' mineralogy and iron content (Bristow et al., 2010). More
816 efforts should be therefore devoted to better characterize the variability of dust spectral optical proper-
817 ties at the regional and sub–regional scale with the aim of better assessing the dust impact on the
818 climate of different areas of the world.

819

820

821 **Data availability**

822 Complex refractive index and single scattering albedo data for the different analyzed samples are pro-
823 vided in Tables 4 and 5 and will be compiled together with aerosol properties from other studies within
824 the Library of Advanced Data Products (LADP) of the EUROCHAMP datacenter (https://data.euro-
825 champ.org). Processed The CESAM data used in this study are immediately available upon request to
826 the contact author and . They will also soon be made available through the Database of Atmospheric
827 Simulation Chamber Studies (DASCS) of the EUROCHAMP datacenter (https://data.eurochamp.org
828 /)EUROCHAMP–2020 data center (https://data.eurochamp.org/). The following IDL routines were used
829 in the analysis: mpfitexy.pro (available at https://github.com/williamsmj/mpfitexy) was used to linearly fit
830 data taking into account uncertainties on both x and y; mie_single.pro (available at
831 http://www.atm.ox.ac.uk/code/mie/mie_single.html) was used for optical calculations using Mie theory;
832 mpcurvefit.pro (available at http://cow.physics.wisc.edu/~craigm/idl/idl.html) was used for size lognor-
833 mal fitting.

834

835 **Author contributions**

836 C. Di Biagio, P. Formenti, Y. Balkanski, and J. F. Doussin designed the experiments and discussed the
837 results. C. Di Biagio performed the experiments and performed the full data analysis with contributions

by P. Formenti, L. Caponi, M. Cazaunau, E. Pangui, and J.F. Doussin. The soil samples used for experiments were collected by M. O. Andreae, K. Kandler, T. Saeed, S. Piketh, D. Seibert, and E. Williams. E. Journet participated to the selection of the soil samples for experiments. S.~~ophie~~ Nowak performed the XRD measurements. C. Di Biagio and P. Formenti wrote the manuscript with comments from all co–authors.

References

Anderson, T. L. and Ogren, J. A.: Determining aerosol radiative properties using the TSI 3563 integrating nephelometer, Aerosol Sci. Technol., 29, 57–69, 1998.

Arimoto, R., Balsam, W., and Schloesslin, C.: Visible spectroscopy of aerosol particles collected on filters: iron–oxide minerals, Atmos. Environ., 36, 89–96, 2002.

Arnott, W., Hamasha, K., Moosmüller, H., Sheridan, P. J. , and Ogren, J. A.: Towards aerosol light–absorption measurements with a 7–wavelength aethalometer: Evaluation with a photoacoustic instrument and 3–wavelength nephelometer, Aerosol Sci. Tech., 39(1), 17–29, 2005.

Balkanski, Y., Schulz, M., Claquin, T., and Guibert, S.: Reevaluation of Mineral aerosol radiative forcings suggests a better agreement with satellite and AERONET data, Atmos. Chem. Phys., 7, 81–95, doi:10.5194/acp–7–81–2007, 2007.

Bangalath, H.K. and Stenchikov, G.: Sensitivity of the Middle East–North African Tropical Rainbelt to Dust Shortwave Absorption: A High–Resolution AGCM Experiment. J. Climate, 29, 7103–7126, https://doi.org/10.1175/JCLI–D–15–0827.1, 2016.

Betzer, P., Carder, K., Duce, R., & Merrill, J.: Long range transport of giant mineral aerosol particles. Nature, 336, 568–571, 1988.

Boucher, O., et al., Clouds and Aerosols. Stocker, T., & Qin, D. (eds), Climate Change 2013: The Physical Science Basis. Contribution of Working Group I to the Fifth Assessment Report of the Intergovernmental Panel on Climate Change. Cambridge Univ. Press, Cambridge, United Kingdom and New York, NY, USA, 2013.

Bretl, S., P. Reutter, C. C. Raible, S. Ferrachat, C. Schnadt Poberaj, L. E. Revell, and U. Lohmann: The influence of absorbed solar radiation by Saharan dust on hurricane genesis, J. Geophys. Res. Atmos., 120, doi:10.1002/2014JD022441, 2015.

Bristow, C. S., Hudson-Edwards, K. A., and Chappell, A.: Fertilizing the Amazon and equatorial Atlantic with West African dust, Geophys. Res. Lett., 37, L14807, doi:10.1029/2010GL043486, 2010.

Caponi, L., Formenti, P., Massabó, D., Di Biagio, C., Cazaunau, M., Pangui, E., Chevaillier, S., Landrot, G., Andreae, M. O., Kandler, K., Piketh, S., Saeed, T., Seibert, D., Williams, E., Balkanski, Y., Prati, P., and Doussin, J.-F.: Spectral- and size-resolved mass absorption efficiency of mineral dust aerosols in the shortwave spectrum: a simulation chamber study, Atmos. Chem. Phys., 17, 7175–7191, https://doi.org/10.5194/acp-17-7175-2017, 2017.

Carrico, C. M., P. Kus, M. J. Rood, P. K. Quinn, and T. S. Bates, Mixtures of pollution, dust, sea salt, and volcanic aerosol during ACE-Asia: Radiative properties as a function of relative humidity, J. Geophys. Res., 108, 8650, doi: 10.1029/2003JD003405, D23, 2003.

Cattrall, C., Carder, K. L., and Gordon, H. R.: Columnar aerosol single-scattering albedo and phase function retrieved from sky radiance over the ocean: Measurements of Saharan dust, J. Geophys. Res.-Atmos., 108(D9), 4287, doi:10.1029/2002JD002497, 2003

Chen, G., Ziemba, L. D., Chu, D. A., Thornhill, K. L., Schuster, G. L., Winstead, E. L., Diskin, G. S., Ferrare, R. A., Burton, S. P., Ismail, S., Kooi, S. A., Omar, A. H., Slusher, D. L., Kleb, M. M., Reid, J. S., Twohy, C. H., Zhang, H., and Anderson, B. E.: Observations of Saharan dust microphysical and optical properties from the Eastern Atlantic during NAMMA airborne field campaign, Atmos. Chem. Phys., 11, 723–740, https://doi.org/10.5194/acp-11-723-2011, 2011.

Chou, C., Formenti, P., Maille, M., Ausset, P., Helas, G., Harrison, M., and Osborne, S.: Size distribution, shape, and composition of mineral dust aerosols collected during the African Monsoon Multidisciplinary Analysis Special Observation Period 0: Dust and Biomass-Burning Experiment field campaign in Niger, January 2006, J. Geophys. Res., 113, D00C10, doi:10.1029/2008jd009897, 2008.

Claquin, T., Schulz, M., and Balkanski, Y.: Modeling the mineralogy of atmospheric dust sources, J. Geophys. Res., 104, 22 243– 22 256, 1999.

Clarke, A. D., Shinozuka, Y. V., Kapustin, N., Howell, S., Huebert, B., Doherty, S., Anderson, T., Covert, D., Anderson, J., Hua, X., Moore II, K. G., McNaughton, C., Carmichael, G., and Weber, R.: Size distributions and mixtures of dust and black carbon aerosol in Asian outflow: Physiochemistry and optical properties, J. Geophys. Res., 109, D15S09, doi:10.1029/2003JD004378, 2004.

Colarco, P. R., Nowottnick, E. P., Randles, C. A., Yi, B., Yang, P., Kim, K.-M., Smith, J. A., and Bardeen, C. G.: Impact of radiatively interactive dust aerosols in the NASA GEOS-5 climate model: Sensitivity to dust particle shape and refractive index, J. Geophys. Res. Atmos., 119, 753–786, doi: 10.1002/2013JD020046, 2014.

Collaud Coen, M., Weingartner, E., Apituley, A., Ceburnis, D., Fierz-Schmidhauser, R., Flentje, H., Henzing, J. S., Jennings, S. G., Moerman, M., Petzold, A., Schmid, O., and Baltensperger, U.: Minimizing light absorption measurement artifacts of the Aethalometer: evaluation of five correction algorithms, Atmos. Meas. Tech., 3, 457–474, doi:10.5194/amt-3-457-2010, 2010.

d'Almeida, G. A., Koepke, P., and Shettle, E.P.: Atmospheric Aerosols: Global Climatology and Radiative Characteristics, A. Deepak Publishing, 561 pp., 1991.

Das, S., S. Dey, S. K. Dash, G. Giuliani, and F. Solmon: Dust aerosol feedback on the Indian summer monsoon: Sensitivity to absorption property, J. Geophys. Res. Atmos., 120, 9642–9652, doi: 10.1002/2015JD023589, 2015.

Denjean, C., Formenti, P., Picquet-Varrault, B., Katrib, Y., Pangui, E., Zapf, P., and Doussin, J. F.: A new experimental approach to study the hygroscopic and optical properties of aerosols: application to ammonium sulphate particles, Atmos. Meas. Tech., 7, 183–197, doi:10.5194/amt-7-183-2014, 2014.

Denjean, C., Cassola, F., Mazzino, A., Triquet, S., Chevaillier, S., Grand, N., Bourrianne, T., Momboisse, G., Sellegri, K., Schwarzenbock, A., Freney, E., Mallet, M., and Formenti, P.: Size distribution and optical properties of mineral dust aerosols transported in the western Mediterranean, Atmos. Chem. Phys., 16, 1081–1104, https://doi.org/10.5194/acp-16-1081-2016, 2016a.

Denjean, C., Formenti, P., Desboeufs, K., Chevaillier, S., Triquet, S., Maillé, M., Cazaunau, M., Laurent, B., Mayol-Bracero, O. L., Vallejo, P., Quiñones, M., Gutierrez-Molina, I. E., Cassola, F., Prati, P., Andrews, E., and

Ogren, J.: Size distribution and optical properties of African mineral dust after intercontinental transport, J. Geophys. Res. Atmos., 121, 7117–7138, https://doi.org/10.1002/2016JD024783, 2016b.

Derimian, Y., Karnieli, A., Kaufman, Y. J., Andreae, M. O., Andreae, T. W., Dubovik, O., Maenhaut, W., and Koren, I.: The role of iron and black carbon in aerosol light absorption, Atmos. Chem. Phys., 8, 3623–3637, 2008.

Di Biagio, C., Formenti P., Styler S. A., Pangui E., and Doussin J. F.: Laboratory chamber measurements of the longwave extinction spectra and complex refractive indices of African and Asian mineral dusts, Geophys. Res. Lett., 41, 6289–6297, doi:10.1002/2014GL060213, 2014a.

Di Biagio, C., Boucher, H., Caquineau, S., Chevaillier, S., Cuesta, J., and Formenti, P.: Variability of the infrared complex refractive index of African mineral dust: experimental estimation and implications for radiative transfer and satellite remote sensing, Atmos. Chem. Phys., 14, 11093–11116, https://doi.org/10.5194/acp-14-11093-2014, 2014b.

Di Biagio, C., Formenti, P., Balkanski, Y., Caponi, L., Cazaunau, M., Pangui, E., Journet, E., Nowak, S., Caquineau, S., Andreae, M. O., Kandler, K., Saeed, T., Piketh, S., Seibert, D., Williams, E., and Doussin, J. F.: Global scale variability of the mineral dust long wave refractive index: a new dataset of in situ measurements for climate modeling and remote sensing, Atmos. Chem. Phys., 17, 1901–1929, https://doi.org/10.5194/acp-17-1901-2017, 2017a.

Di Biagio, C., Formenti, P., Cazaunau, M., Pangui, E., Marchand, N., and Doussin, J. F.: Aethalometer multiple scattering correction C_{ref} for mineral dust aerosols, Atmos. Meas. Tech., 10, 2923–2939, https://doi.org/10.5194/amt-10-2923-2017, 2017b.

Dubovik, O., Holben, B. N., and Eck, T. F. et al.: Variability of absorption and optical properties of key aerosol types observed in worldwide locations, J. Atmos. Sci., 59, 590– 608, 2002.Dunion, J. P., and C. S. Velden: The impact of the Saharan air layer on Atlantic tropical cyclone activity, Bull. Am. Meteorol. Soc., *85*(3), 353. Meteoro:10.1175/BAMS-85-3-353, 2004.

Engelbrecht, J. P., Moosmüller, H., Pincock, S., Jayanty, R. K. M., Lersch, T., and Casuccio, G.: Technical note: Mineralogical, chemical, morphological, and optical interrelationships of mineral dust re suspensions, Atmos. Chem. Phys., 16, 10809–10830, https://doi.org/10.5194/acp-16-10809-2016, 2016.Feng, Q., P. Yang, G. W. Kattawar, C. N. Hsu, S. C. Tsay, and I. Laszlo: Effects of particle nonsphericity and radiation polarization on retrieving dust properties from MODIS observations, J. Aerosol Sci., 40(9), 776–789, doi:10.1016/j.jaerosci.2009.05.001, 2009.

Flores, J. M., Trainic, M., Borrmann, S., and Rudich, Y.: Effective broadband refractive index retrieval by a white light optical particle counter, Phys. Chem. Chem. Phys., 11, 7943–7950, 2009.

Formenti, P., Andreae, M. O., Lange, L., Roberts, G., Cafmeyer, J., Rajta, I., Maenhaut, W., Holben, B. N., Artaxo, P., and Lelieveld, J.: Saharan dust in Brazil and Suriname during the Large Scale Biosphere–Atmosphere Experiment in Amazonia (LBA) – Cooperative LBA Regional Experiment (CLAIRE) in March 1998, J. Geophys. Res., 106, 14919–14934, https://doi.org/10.1029/2000jd900827, 2001.

Formenti, P., Rajot, J. L., Desboeufs, K., Said, F., Grand, N., Chevaillier, S., and Schmechtig, C.: Airborne observations of mineral dust over western Africa in the summer Monsoon season: spatial and vertical variability of physico chemical and optical properties, Atmos. Chem. Phys., 11, 6387–6410, doi:10.5194/acp-11-6387-2011, 2011.

Formenti, P., Caquineau, S., Desboeufs, K., Klaver, A., Chevaillier, S., Journet, E., and Rajot, J. L.: Mapping the physicochemical properties of mineral dust in western Africa: mineralogical composition, Atmos. Chem. Phys., 14, 10663–10686, https://doi.org/10.5194/acp-14-10663-2014, 2014a.

Formenti, P., Caquineau, S., Chevaillier, S., Klaver, A., Desboeufs, K., Rajot, J. L., Belin, S., and Briois, V.: Dominance of goethite over hematite in iron oxides of mineral dust from western Africa: quantitative partitioning by X ray Absorption Spectroscopy, J. Geophys. Res. Atmos., 119, 12740–12754, https://doi.org/10.1002/2014JD021668, 2014b.

Gasteiger, J., Wiegner, M., Groß, S., Freudenthaler, V., Toledano, C., Tesche, M., and Kandler, K.: Modelling lidar relevant optical properties of complex mineral dust aerosols, Tellus B, 63, 725–741, https://doi.org/10.1111/j.1600-0889.2011.00559.x, 2011.

Ginoux, P., Prospero, J. M., Gill, T. E., Hsu, N. C., and Zhao, M.: Global scale attribution of anthropogenic and natural dust sources and their emission rates based on MODIS Deep Blue aerosol products, Rev. Geophys., 50, RG3005, doi:10.1029/2012RG000388, 2012.

Green, R. O.; Mahowald, N. M.; Clark, R. N.; Ehlmann, B. L.; Ginoux, P. A.; Kalashnikova, O. V.; Miller, R. L.; Okin, G.; Painter, T. H.; Pérez García–Pando, C.; Realmuto, V. J.; Swayze, G. A.; Thompson, D. R.; Middleton, E.; Guanter, L.; Ben Dor, E.; Phillips, B. R. (2018) NASA's Earth Surface Mineral Dust Source Investigation. American Geophysical Union, Fall Meeting 2018, abstract #A24D–01.

Haywood, J., Francis, P., Osborne, S., Glew, M., Loeb, N., Highwood, E., Tanré, D., Myhre, G., Formenti, P., and Hirst, E.: Radiative properties and direct radiative effect of Saharan dust measured by the C-130 aircraft during SHADE: 1. Solar spectrum, J. Geophys. Res., 108(D18), 8577, doi:10.1029/2002JD002687, 2003.

Hess, M., Koepke, P., and Schult, I.: Optical properties of aerosols and clouds: The software package OPAC, Bull. Am. Meteorol. Soc, 79, 831–844, 1998.

Highwood, E. J., and Ryder, C. L.: Radiative effects of dust. In Mineral Dust: A Key Player in the Earth System. P. Knippertz, and J.-B.W. Stuut, Eds. Springer, 267-286, doi:10.1007/978-94-017-8978-3_13, 2014.

Hsu, N. C., Tsay, S.-C., King, M. D., and Herman, J. R.: Aerosol properties over bright-reflecting source regions, IEEE T. Geosci. Remote Sens., 42, 557–569, 2004.

Iwasaka, Y., Shi, G.-Y., Shen, Z., Kim, Y. S., Trochkin, D., Matsuki, A., Zhang, D., Shibata, T., Nagatani, M., and Nakata, H.: Nature of atmospheric aerosols over the desert area in the Asian continent: chemical state and number concentration of particles measured at Dunhuang, China, Water Air Soil Poll., 3, 129–145, 2003

Jeong, G. Y., J. Y. Kim, J. Seo, G. M. Kim, H. C. Jin, and Y. Chun: Long-range transport of giant particles in Asian dust identified by physical, mineralogical, and meteorological analysis, Atmos. Chem. Phys., 14(1), 505–521, doi:10.5194/acp-14-505-2014, 2014.

Jin, Q., Zang, Z.-L., and Wei, J.: High sensitivity of Indian summer monsoon to Middle East dust absorptive properties, Sci. Rep, 6:30690, doi: 10.1038/srep30690, 2016.

Johnson, B. T. and Osborne, S. R.: Physical and optical properties of mineral dust aerosol measured by aircraft during the GERBILS campaign. Q.J.R. Meteorol. Soc., 137: 1117-1130. doi:10.1002/qj.777, 2011.

Journet, E., Balkanski, Y., and Harrison, S. P.: A new data set of soil mineralogy for dust-cycle modeling, Atmos. Chem. Phys., 14, 3801-3816, doi:10.5194/acp-14-3801-2014, 2014.

Kalashnikova, O. V. and Sokolik, I. N.: Modeling the radiative properties of nonspherical soil-derived mineral aerosols, J. Quant. Spectrosc. Ra., 87, 137–166, 2004.

Kandler, K., Schütz, L., Deutscher, C., Ebert, M., Hofmann, H., Jäckel, S., Jaenicke, R., Knippertz, P., Lieke, K., Massling, A., Petzold, A., Schladitz, A.,Weinzierl, B.,Wiedensohler, A., Zorn, S., and Weinbruch, S.: Size distribution, mass concentration, chemical and mineralogical composition and derived optical parameters of the boundary layer aerosol at Tinfou, Morocco, during SAMUM 2006, Tellus B, 61, 32–50, doi:10.1111/j.1600-0889.2008.00385.x, 2009.

Karickhoff, S.W. and Bailey, G.W. 1973. Optical absorption spectra of clay minerals. Clay Clay Miner., 21, 59–70.Kaufman, Y. J.: Satellite sensing of aerosol absorption, J. Geophys. Res., 92, 4307–4317, 1987.

Kaufman, Y. J., Tanr'e, D., Dubovik, O., Karnieli, A., and Remer, L. A.: Absorption of sunlight by dust as inferred from satellite and ground-based remote sensing, Geophys. Res. Lett., 28, 1479–1482, 2001.

Koepke, P., Gasteiger, J., and Hess, M.: Technical Note: Optical properties of desert aerosol with non-spherical mineral particles: data incorporated to OPAC, Atmos. Chem. Phys., 15, 5947-5956, https://doi.org/10.5194/acp-15-5947-2015, 2015.

Kok, J.F., D.A. Ridley, Q. Zhou, R.L. Miller, C. Zhao, C.L. Heald, D.S. Ward, S. Albani, and K. Haustein: Smaller desert dust cooling effect estimated from analysis of dust size and abundance. Nature Geosci., 10, no. 4, 274-278, doi:10.1038/ngeo2912, 2017.

Konaré, A., Zakey, A. S., Solmon, F., Giorgi, F., Rauscher, S., Ibrah, S., and Bi, X.: A regional climate modeling study of the effect of desert dust on the West African monsoon, J. Geophys. Res., 113, D12206, doi:10.1029/2007JD009322, 2008.

Koven, C.D., and Fung, I.: Inferring dust composition from wavelength-dependent absorption in Aerosol Robotic Network (AERONET) data. J Geophys Res 111, D14205. doi:10.1029/2005JD006678, 2006.

Lafon, S., Sokolik, I. N., Rajot, J. L., Caquineau, S., and Gaudichet, A.: Characterization of iron oxides in mineral dust aerosols: Implications for light absorption, J. Geophys. Res., 111, D21207, doi:10.1029/2005jd007016, 2006.

Liao, H. and Seinfeld, J. H.: Radiative forcing by mineral dust aerosols: sensitivity to key variables, J. Geophys. Res., 103(D24), 31 637–31 646, doi:10.1029/1998JD200036, 1998.

Lide, D. R.: CRC Handbook of Chemistry and Physics 1991–1992, CRC Press, Boca Raton, Florida, 1992.

Linke, C., Möhler, O., Veres, A., Mohácsi, A., Bozóki, Z., Szabó, G., and Schnaiter, M., Optical properties and mineralogical composition of different Saharan mineral dust samples: a laboratory study, Atmos. Chem. Phys., 6, 3315–3323, 2006.

Lu, H., Wei, W., Liu, M., Wu, X., Mou, S., and Han, Q.: Quantification and semi-quantification of iron-oxide minerals in aerosol particles in the hinterland of Taklimakan Desert, Scientia Geographica Sinica, 31, 969–975, 2011.

Maring, H., Savoie, D. L., Izaguirre, M. A., McCormick, C., Arimoto, R., Prospero, J. M., and Pilinis, C.: Aerosol physical and optical properties and their relationship to aerosol composition in the free troposphere at izana, tenerife, canary islands, during July 1995, J. Geophys. Res.-Atmos., 105, 14677–14700, 2000.

Maring, H., Savoie, D. L., Izaguirre, M. A., Custals, L., and Reid, J. S.: Mineral dust aerosol size distribution change during atmospheric transport, J. Geophys. Res., 108, 8592, doi:10.1029/2002jd002536, 2003.

McConnell, C. L., Highwood, E. J., Coe, H., Formenti, P., Anderson, B., Osborne, S., Nava, S., Desboeufs, K., Chen, G., and Harrison, M. A. J.: Seasonal variations of the physical and optical characteristics of Saharan dust: Results from the Dust Outflow and Deposition to the Ocean (DODO) experiment, J. Geophys. Res., 113, D14S05, doi:10.1029/2007jd009606, 2008.

McConnell, C. L., Formenti, P., Highwood, E. J., and Harrison, M. A. J.: Using aircraft measurements to determine the refractive index of Saharan dust during the DODO Experiments, Atmos. Chem. Phys., 10, 3081–3098, doi:10.5194/acp-10-3081-2010, 2010.

Miller, R. L., I. Tegen, and J. Perlwitz: Surface radiative forcing by soil dust aerosols and the hydrologic cycle, J. Geophys. Res., 109, D04203, doi:10.1029/2003JD004085, 2004.

Miller, R. L., Knippertz, P., Pérez García-Pando, C., Perlwitz, J. P., and Tegen, I.: Impact of dust radiative forcing upon climate. In Mineral Dust: A Key Player in the Earth System. P. Knippertz, and J.-B.W. Stuut, Eds. Springer, 327-357, doi:10.1007/978-94-017-8978-3_13, 2014.

Mishchenko, M., A. Lacis, B. Carlson, and L. Travis: Nonsphericity of dust-like tropospheric aerosols—Implications for aerosol remotesensing and climate modeling, Geophys. Res. Lett., 22(9), 1077–1080, 1995.

Mogili, P. K., Yang, K. H., Young, M. A., Kleiber, P. D., and Grassian, V. H.: Environmental aerosol chamber studies of extinction spectra of mineral dust aerosol components: Broadband IR–UV extinction spectra, J. Geophys. Res.–Atmos., 112, D21204, doi:10.1029/2007JD008890, 2007.

Moosmüller, H., Engelbrecht, J. P., Skiba, M., Frey, G., Chakrabarty, R.K., and Arnott, W.P., Single scattering albedo of fine mineral dust aerosols controlled by iron concentration, J. Geophys. Res., 117, D11210, doi:10.1029/2011JD016909, 2012.

Müller, T., Schladitz, A., Massling, A., Kaaden, N., Kandler, K., and coauthors: Spectral absorption coefficients and imaginary parts of refractive indices of Saharan dust during SAMUM-1. Tellus 61B, 79–95, 2009.

Müller, T., Schladitz, A., Kandler, K., and Wiedensohler, A.: Spectral particle absorption coefficients, single scattering albedos and imaginary parts of refractive indices from ground based in situ measurements at Cape Verde Island during SAMUM-2, Tellus B, 63, 573–588, doi:10.1111/j.1600-0889.2011.00572.x, 2011.

Myhre, G. and Stordal, F.: Global sensitivity experiments of the radiative forcing due to mineral aerosols, J. Geophys. Res., 106(D16), 18 193–18 204, doi:10.1029/2000JD900536, 2001.

Nickovic, S., Vukovic, A., Vujadinovic, M., Djurdjevic, V., and Pejanovic, G.: Technical Note: High-resolution mineralogical database of dust-productive soils for atmospheric dust modeling, Atmos. Chem. Phys., 12, 845–855, doi:10.5194/acp-12-845-2012, 2012.

Nousiainen, T. and Kandler, K.: Light scattering by atmospheric mineral dust particles, in: Light Scattering Reviews 9, edited by: Kokhanovsky, A. A., Springer Praxis Books, Springer, Berlin, Heidelberg, 3–52, doi:10.1007/978-3-642-37985-7, 2015. 16863, 16864, 16866

Okada, K., Heintzenberg, J., Kai, K., Qin, Y., 2001. Shape of atmospheric mineral particles collected in three Chinese arid-regions. Geophys. Res. Lett. 28 (16), 3123–3126

Osborne, S.R., Johnson, B.T., Haywood, J.M., Baran, A.J., Harrison, M.A.J., and McConnell, C.L.: Physical and optical properties of mineral dust aerosol during the Dust and Biomass-burning Experiment, J. Geophys. Res., 113, D00C03, doi:10.1029/2007jd009551, 2008.

Otto, S., Bierwirth, E., Weinzierl, B., Kandler, K., Esselborn, M., Tesche, M., Schladitz, A.,Wendisch, M., and Trautmann, T.: Solar radiative effects of a Saharan dust plume observed during SAMUM assuming spheroidal model particles, Tellus B, 61, 270–296, doi:10.1111/j.1600-0889.2008.00389.x, 2009.

Patterson, E.M., Filette, D. A., and Stockton, B. H.: Complex index of refraction between 300 and 700 nm for Saharan aerosols, J. Geophys. Res., 82, 3153–3160, 1977.

Perlwitz, J. P., Pérez García-Pando, C., and Miller, R. L.: Predicting the mineral composition of dust aerosols – Part 1: Representing key processes, Atmos. Chem. Phys., 15, 11593-11627, https://doi.org/10.5194/acp-15-11593-2015, 2015a.

Perlwitz, J. P., Pérez García-Pando, C., and Miller, R. L.: Predicting the mineral composition of dust aerosols – Part 2: Model evaluation and identification of key processes with observations, Atmos. Chem. Phys., 15, 11629-11652, https://doi.org/10.5194/acp-15-11629-2015, 2015b.

Petzold, A., Schloesser, H., Sheridan, P. J., Arnott, W. P., Ogren, J. A., and Virkkula, A.: Evaluation of Multi-angle Absorption Photometry for Measuring Aerosol Light Absorption, Aerosol Sci. Technol., 39, 40–51, 2005.

Petzold, A., Rasp, K., Weinzierl, B., Esselborn, M., Hamburger, T., Dornbrack, A., Kandler, K., Schutz, L., Knippertz, P., Fiebig, M., Virkkula, A., Saharan dust absorption and refractive index from aircraft-based observations during SAMUM 2006, Tellus B 61: 118–130, 2009.

Petzold, A., Onasch, T., Kebabian, P., and Freedman, A.: Intercomparison of a Cavity Attenuated Phase Shift-based extinction monitor (CAPS PMex) with an integrating nephelometer and a filter-based absorption monitor, Atmos. Meas. Tech., 6, 1141–1151, doi:10.5194/amt-6-1141-2013, 2013.Räisänen, P., P. Haapanala, C. E. Chung, M. Kahnert, R. Makkonen, J. Tonttila, and T. Nousiainen: Impact of dust particle non-sphericity on climate simulations, Q. J. R. Meteorol. Soc., 139, 2222–2232, doi:10.1002/qj.2084, 2012.

Räisänen, P., P. Haapanala, C. E. Chung, M. Kahnert, R. Makkonen, J. Tonttila, and T. Nousiainen: Impact of dust particle non–sphericity on climate simulations, Q. J. R. Meteorol. Soc., 139, 2222‑2232, doi:10.1002/qj.2084, 2012.

Rajot, J. L., Formenti, P., Alfaro, S., Desboeufs, K., Chevaillier, S., Chatenet, B., Gaudichet, A., Journet, E., Maricorena, B., Triquet, S., Maman, A., Mouget, N., and Zakou, A.: AMMA dust experiment: an overview of measurements performed during the dry season special observation period (SOP0) at the Banizoumbou (Niger) supersite, J. Geophys. Res., 113, D00C14, doi:10.1029/2008jd009906, 2008.

Redmond, H. E., Dial, K. D., and Thompson, J.E.: Light scattering and absorption by wind-blown dust: theory, measurement and recent data, Aeolian Res., 2, 5–26, 2010.

Reid, E. A., Reid, J. S., Meier, M. M., Dunlap, M. R., Cliff, S. S., Broumas, A., Perry, K., and Maring, H.: Characterization of African dust transported to Puerto Rico by individual particle and size segregated bulk analysis, J. Geophys. Res., 108, 8591, doi:10.1029/2002jd002935, 2003.

Ridley, D. A., Heald, C. L., Kok, J. F., and Zhao, C.: An observationally constrained estimate of global dust aerosol optical depth, Atmos. Chem. Phys., 16, 15097–15117, https://doi.org/10.5194/acp-16-15097-2016, 2016.

Rocha-Lima, A., Martins, J. V., Remer, L. A., Todd, M., Marsham, J. H., Engelstaedter, S., Ryder, C. L., Cavazos-Guerra, C., Artaxo, P., Colarco, P., and Washington, R.: A detailed characterization of the Saharan dust collected during the Fennec campaign in 2011: in situ ground-based and laboratory measurements, Atmos. Chem. Phys., 18, 1023–1043, https://doi.org/10.5194/acp-18-1023-2018, 2018.

Ryder, C. L., Highwood, E. J., Rosenberg, P. D., Trembath, J., Brooke, J. K., Bart, M., Dean, A., Crosier, J., Dorsey, J., Brindley, H., Banks, J., Marsham, J. H., McQuaid, J. B., Sodemann, H., and Washington, R.: Optical properties of Saharan dust aerosol and contribution from the coarse mode as measured during the Fennec 2011 aircraft campaign, Atmos. Chem. Phys., 13, 303–325, doi:10.5194/acp-13-303-2013, 2013a.

Ryder, C. L., Highwood, E. J., Lai, T. M., Sodemann, H., and Marsham J. H.: Impact of atmospheric transport on the evolution of microphysical and optical properties of Saharan dust, Geophys. Res. Lett., 40, 2433–2438, doi:10.1002/grl.50482, 2013b.

Ryder, C. L., Marenco, F., Brooke, J. K., Estelles, V., Cotton, R., Formenti, P., McQuaid, J. B., Price, H. C., Liu, D., Ausset, P., Rosenberg, P. D., Taylor, J. W., Choularton, T., Bower, K., Coe, H., Gallagher, M., Crosier, J., Lloyd, G., Highwood, E. J., and Murray, B. J.: Coarse–mode mineral dust size distributions, composition and optical properties from AER–D aircraft measurements over the tropical eastern Atlantic, Atmos. Chem. Phys., 18, 17225–17257, https://doi.org/10.5194/acp–18–17225–2018, 2018.

Samset, B. H., Stjern, C. W., Andrews, E., Kahn, R. A., Myhre, G., Schulz, M., and Schuster, G. L.: Aerosol Absorption: Progress Towards Global and Regional Constraints, Curr. Clim. Change Rep., 4, 65–83, 2018.

Saturno, J., Pöhlker, C., Massabo, D., Brito, J., Carbone, S., Cheng, Y. F., Chi, X. G., Ditas, F., de Angelis, I. H., Moran-Zuloaga, D., Pohlker, M. L., Rizzo, L. V., Walter, D., Wang, Q. Q., Artaxo, P., Prati, P., and Andreae, M. O., Comparison of different Aethalometer correction schemes and a reference multi-wavelength absorption technique for ambient aerosol data: Atmos. Meas. Tech., 10, 2837–2850, doi:10.5194/amt-10-2837-2017, 2017.

Scanza, R. A., Mahowald, N., Ghan, S., Zender, C. S., Kok, J. F., Liu, X., Zhang, Y., and Albani, S.: Modeling dust as component minerals in the Community Atmosphere Model: development of framework and impact on radiative forcing, Atmos. Chem. Phys., 15, 537–561, doi:10.5194/acp-15-537-2015, 2015.

Scheuvens, D., Schütz, L., Kandler, K., Ebert, M., and Weinbruch, S.: Bulk composition of northern African dust and its source sediments – A compilation, Earth-Sci. Rev., 116, 170–194, https://doi.org/10.1016/j.earscirev.2012.08.005, 2013.

Schladitz, A., M¨uller, T., Kaaden, N., Massling, A., Kandler, K., Ebert, M., Weinbruch, S., Deutscher, C., and Wiedensohler, A.: In situ measurements of optical properties at Tinfou (Morocco) during the Saharan Mineral Dust Experiment SAMUM 2006, Tellus B, 61, 64–78, doi:10.1111/j.1600-0889.2008.00397.x, 2009.

Shen, Z., Cao, J., Zhang, X., Arimoto, R., Ji, J., Balsam, W., Wang, Y., Zhang, R., and Li, X.: Spectroscopic analysis of iron-oxide minerals in aerosol particles from northern China, Sci. Total Environ., 367, 899–907, 2006.

Shettle, E. P., and Fenn, R.W.: Models for the Aerosols of the Lower Atmosphere and the Effects of Humidity Variations on Their Optical Properties, AFGL-TR-79-0214, ADA085951, 1979.

Shin, S.-K., Tesche, M., Kim, K., Kezoudi, M., Tatarov, B., Müller, D., and Noh, Y.: On the spectral depolarisation and lidar ratio of mineral dust provided in the AERONET version 3 inversion product, Atmos. Chem. Phys., 18, 12735–12746, https://doi.org/10.5194/acp-18-12735-2018, 2018.

Sinyuk, A., Torres, O., and Dubovik, O., Combined use of satellite and surface observations to infer the imaginary part of refractive index of Saharan dust, Geophys. Res. Lett., 30(2), 1081, doi:10.1029/2002GL016189, 2003.

Sokolik, I., and Toon, O.: Incorporation of mineralogical composition into models of the radiative properties of mineral aerosol from UV to IR wavelengths, J. Geophys. Res., 104(D8), 9423–9444, 1999.

Sokolik, I.N., Andronova, A.V., and Jonhson, T.C.: Complex refractive index of atmospheric dust aerosols, Atmos. Environ., 16, 2495–2502, 1993.

Solmon, F., Mallet, M., Elguindi, N., Giorgi, F., Zakey, A. and Konaré, A.: Dust aerosol impact on regional precipitation over western Africa, mechanisms and sensitivity to absorption properties, Geophys. Res. Lett., 35, L24705, doi:10.1029/2008GL035900, 2008.

Sorribas, M. , Olmo, F. J., Quirantes, A. , Lyamani, H. , Gil-Ojeda, M. , Alados-Arboledas, L. and Horvath, H. (2015), Role of spheroidal particles in closure studies for aerosol microphysical–optical properties. Q.J.R. Meteorol. Soc., 141: 2700–2707. doi:10.1002/qj.2557.

Stegmann, P. G., Yang, P., A regional, size-dependent, and causal effective medium model for Asian and Saharan mineral dust refractive index spectra, J. Aer. Sci., 114, 327–341, 2017.

Strong, J. D. O., Vecchi, G. A., & Ginoux, P.: The climatological effect of Saharan dust on global tropical cyclones in a fully coupled GCM. Journal of Geophysical Research: Atmospheres, 123, 5538–5559. https://doi-org.insu.bib.cnrs.fr/10.1029/2017JD027808, 2018

Su, L., and Toon O.B.: Saharan and Asian dust: similarities and differences determined by CALIPSO, AERONET, and a coupled climate-aerosol microphysical model, Atmos. Chem. Phys.; 11, 3263–3280, 2011.

Todd, M. C., R. Washington, J. V. Martins, O. Dubovik, G. Lizcano, S. M'Bainayel, and S. Engelstaedter, Mineral dust emission from the Bodélé´ Depression, northern Chad, during BoDEx 2005, J. Geophys. Res., 112, D06207, doi:10.1029/2006JD007170, 2007.

Toon, O. B., Pollack, J. B., and Khare, B. N.: The optical constants of several atmospheric aerosol species: ammonium sulphate, aluminum oxide, and sodium chloride, J. Geophys. Res., 81, 5733–5748, 1976.

Uno, I., K. Eguchi, K. Yumimoto, T. Takemura, A. Shimizu, M. Uematsu, Z. Liu, Z. Wang, Y. Hara, and N. Sugimoto, Asian dust transported one full circuit around the globe, Nat. Geosci,2, 557–560, doi:10.1038/ngeo583, 2009.

Vinoj, V. et al. Short-term modulation of Indian summer monsoon rainfall by West Asian dust. Nature Geoscience 7, 308–313, 2014.

Volz, F. E.: Longwave refractive index of atmospheric aerosol substances, Appl. Optics, 11, 755–759, 1972.

Wang, J., Doussin, J. F., Perrier, S., Perraudin, E., Katrib, Y., Pangui, E., and Picquet-Varrault, B.: Design of a new multi-phase experimental simulation chamber for atmospheric photosmog, aerosol and cloud chemistry research, Atmos. Meas. Tech., 4, 2465–2494, 2011.

Wagner, R., Ajtai, T., Kandler, K., Lieke, K., Linke, C., Müller, T., Schnaiter, M., and Vragel, M.: Complex refractive indices of Saharan dust samples at visible and near UV wavelengths: a laboratory study, Atmos. Chem. Phys., 12, 2491–2512, doi:10.5194/acp-12-2491-2012, 2012.

Weingartner, E., Saathoff, H., Schnaiter, M., Streit, N., Bitnar, B., and Baltensperger, U.: Absorption of light by soot particles: determination of the absorption coefficient by means of aethalometers, J. Aerosol Sci., 34, 1445–1463, 2003.

Weinzierl, B., Petzold, A., Esselborn, M., Wirth, M., Rasp, K., Kandler, K., Schutz, L., Koepke, P., and Fiebig, M.: Airborne measurements of dust layer properties, particle size distribution and mixing state of Saharan dust during SAMUM 2006, Tellus, 61B, 96–117, doi:10.1111/j.1600-0889.2008.00392.x, 2009.

Weinzierl, B., Sauer, D., Esselborn, M., Petzold, A., Veira, A., Rose, M., Mund, S.,Wirth, M., Ansmann, A., Tesche, M., Gross, S., and Freudenthaler, V.: Microphysical and optical properties of dust and tropical biomass burning aerosol layers in the Cape Verde region—an overview of the airborne in situ and lidar measurements during SAMUM-2, Tellus B, 63, 589–618, doi:10.1111/j.1600-0889.2011.00566.x, 2011.

Weinzierl, B. et al. (2009), Airborne measurements of dust layer properties, particle size distribution and mixing state of Saharan dust during SAMUM 2006. Tellus– 61B, 96–117.

Yi, B., C. N. Hsu, P. Yang, and S.-C. Tsay: Radiative transfer simulation of dust-like aerosols uncertainties from particle shape and refractive index, J. Aerosol Sci., 42(10), 631–644, doi:10.1016/j.jaerosci.2011.06.008, 2011.

Yoshida, M. and Murakami, H.: Dust absorption averaged over the Sahara inferred from moderate resolution imaging spectroradiometer data, Appl. Opt., 47, 1995–2003, 2008.

1222
1223   Yoshioka, M., Mahowald, N.M., Conley, A.J., Collins, W.D., Fillmore, D.W., Zender, C.S., and Coleman, D.B.: Im-
1224   pact of desert dust radiative forcing on sahel precipitation: Relative importance of dust compared to sea surface
1225   temperature variations, vegetation changes, and greenhouse gas warming, J. Clim., 20, 1445– 1467, 2007.
1226
1227
1228
1229
1230
1231
1232
1233
1234
1235
1236
1237
1238
1239
1240
1241
1242
1243
1244
1245
1246
1247
1248
1249
1250
1251
1252
1253
1254
1255
1256
1257
1258
1259

Table 1. Measured and retrieved quantities and their estimated ~~relative~~ uncertainties. For further de-
tails, refer to Sect. 2, as well DB17 and C17.

Parameter		Time resolution	~~Relative u~~Uncertainty	Uncertainty calculation	Comments
Optical SW	Scattering coefficient at 450, 550, and 700 nm, $\beta_{sca}(\lambda)$	*10–min data*	5–12%	Quadratic combination of photon counting and gas calibration uncertainty (5%), angular corrections uncertainty (<5%) and standard deviation over 10–min intervals (2-–10%).	The uncertainty on $\beta_{sca}(\lambda)$ usually decreases with increasing dust residence time in the chamber as a result of the reduction of the coarse component.
	Absorption coefficient at 370, 470, 520, 590, 660, 880, and 950 nm, $\beta_{abs}(\lambda)$	*10–min data*	22–30% at 370 nm 23–87% at 950 nm	Error propagation formula[1] on Eq. (2) considering the uncertainties on $\beta_{ATT}(\lambda)$ from 10–min fitting procedure (error propagation formula[1] on Eq. 1, ~20%), and uncertainties on $\alpha(\lambda)$ (1%), $\beta_{sca}(\lambda)$ (5–12%), C_{ref} (10%), and R (1–10%).	
	Extinction coefficient, $\beta_{ext}(\lambda) = \beta_{sca}(\lambda) + \beta_{abs}(\lambda)$	*10–min data*	~25%	Sum of $\beta_{sca}(\lambda)$ and $\beta_{abs}(\lambda)$ uncertainties	
	Single Scattering Albedo, SSA (λ) = $\beta_{sca}(\lambda)$ / ($\beta_{sca}(\lambda) + \beta_{abs}(\lambda)$)	*10–min data*	9–12%	Error propagation formula[1] considering single uncertainties on β_{sca} and β_{abs}.	
	Single Scattering Albedo, SSA (λ) = $(1+1/m(\lambda))^{-1}$	*Experiment averaged*	1–12% at 370 nm 1–3% at 950 nm	Error propagation formula[1] on Eq. (6) considering the uncertainty on $m(\lambda)$, i.e., the slope of the linear fit between β_{sca} and β_{abs} over the whole duration of each experiment.	
	Complex refractive index (n-–ik)	*10–min data*	<5% for n <50% for k	Deviations of the values of n and k retrieved in the sensitivity study (see Sect. 3.2) with respect to those obtained in the first inversions were assumed to correspond to the one standard deviation uncertainty to 10–min retrieved values.	
	Complex refractive index (n-–ik)	*Experiment averaged*	<8% for n 13–75 % for k	Quadratic combination of the standard deviation of n and k over the experiment and the deviation on the experiment–averaged values between those obtained from central inversions and inversions using input data ± their uncertainty.	
Size distribution	SMPS geometrical diameter (D_g), $D_g = D_m / \chi$	–	~6%	Error propagation formula[1] considering the uncertainty on the estimated shape factor χ (~6%)	The electrical mobility to geometrical diameter conversion was performed by assuming for dust a dynamic shape factor of 1.75 ± 0.10, as

31

					determined by SMPS–SkyGrimm comparison in their overlapping range (see DB17)
	SkyGrimm geometrical diameter (D_g)	–	<15.2%	Standard deviation of the D_g values obtained for different refractive indices values used in the optical to geometrical conversion	The conversion of optical to geometrical diameters for the SkyGrimm and the WELAS was performed by ~~taking into account the visible complex refractive index of dust aerosols. Optical calculations were computed at the SkyGrimm operating wavelength (0.655 µm) and over the spectral range of the WELAS (0.35 to 0.7 µm) using Mie theory for spherical particles by fixing n at 1.47, 1.50, and 1.53, and by varying k in steps of 0.001 between 0.001 and 0.005.~~ ~~Mie calculations by varying the dust refractive index in the range 1.47–1.53 for the real part and 0.001–0.005 for the imaginary part.~~ Then D_g is set at the mean ± 1 standard deviation of the values obtained for the different values of n and k ~~(see DB17)~~ ~~(see DB17)~~. Refractive index is assumed to be constant with particle size and wavelength–independent.
	WELAS geometrical diameter (D_g)	–	<7%	The same as for the SkyGrimm	
	$(dN/dlogD)_{SWoptics}$	10–min data	~20–90%	Error propagation formula[1] considering the $dN/dlogD_g$ st. dev. over 10–min and the uncertainty on particle loss function along sampling tubes $L(D_g)$ (~50% at 2 µm, ~10% at 8 µm)	The uncertainty of $L(D_g)$ was estimated with a sensitivity study by varying the values of the input parameters to the Particle Loss Calculator software within their uncertainties (see DB17)
	$D_{eff,fine}$	10–min data	<5%	Deviation obtained by repeating the calculations by using the size distribution ± its uncertainty.	
	$D_{eff,coarse}$	10–min data	5–40%		
Mineralogical composition	Elemental iron mass concentration ($MC_{Fe\%}$)	Experiment averaged	10%		
	Iron oxides mass concentration ($MC_{Fe-ox\%}$)	Experiment averaged	15%	Uncertainties calculated as discussed in DB17 and C17	
	Goethite mass concentration ($MC_{Goet\%}$)	Experiment averaged	<10%		
	Hematite mass concentration ($MC_{Hem\%}$)	Experiment averaged	<10%		

1263   [1] $\sigma_f = \sqrt{\sum_{i=1}^{n}\left(\dfrac{\partial f}{\partial x_i}\sigma_{x_i}\right)^2}$

1264

1265

1266
1267
1268
1269
1270
1271
1272
1273
1274
1275
1276
1277
1278

1279 **Table 2.** Summary of information on the soil samples and sediments used in this study.

1280
1281

Geographical area	Sample	Coordinates	Desert area
Northern Africa – Sahara	Tunisia	33.02°N, 10.67°E	Maouna
	Morocco	31.97°N, 3.28°W	east of Ksar Sahli
	Libya	27.01°N, 14.50°E	Sebha
	Algeria	23.95°N, 5.47°E	Ti—n—Tekraouit
	Mauritania	20.16°N, 12.33°W	east of Aouinet Nchir
Sahel	Niger	13.52°N, 2.63°E	Banizoumbou
	Mali	17.62°N, 4.29°W	Dar el Beida
	Bodélé	17.23°N, 19.03°E	Bodélé depression
Eastern Africa and the Middle East	Ethiopia	7.50°N, 38.65°E	Lake Shala National Park
	Saudi Arabia	27.49°N, 41.98°E	Nefud
	Kuwait	29.42°N, 47.69°E	Kuwaiti
Eastern Asia	Gobi	39.43°N, 105.67°E	Gobi
	Taklimakan	41.83°N, 85.88°E	Taklimakan
North America	Arizona	33.15 °N, 112.08°W	Sonoran
South America	Atacama	23.72°S, 70.40°W	Atacama
	Patagonia	50.26°S, 71.50°W	Patagonia
Southern Africa	Namib—1	21.24°S, 14.99°E	Namib
	Namib—2	19.00°S, 13.00°E	Namib
Australia	Australia	31.33°S, 140.33°E	Strzelecki

1282
1283

1284 **Table 3**. Chemical characterization of the dust aerosols in the $PM_{10.6}$ size fraction. Column 3 shows

1285 $MC_{Fe\%}$, the fractional mass of elemental iron with respect to the total dust mass concentration (±10 %

1286 relative uncertainty), and column 4 reports $MC_{Fe-ox\%}$, the mass fraction of iron oxides with respect to the

1287 total dust mass concentration (±15 % relative uncertainty) and its speciation in hematite $MC_{Hem\%}$ and

1288 goethite $MC_{Goeth\%}$ (<±10% relative uncertainty). The iron oxide measurements were not made on the

1289 Taklimakan sample. Mean values and standard deviations based on single sample data are reported

1290 for the full dataset.

1291

Geographical area	Sample	$MC_{Fe\%}$	$MC_{Fe-ox\%}$	$MC_{Hem\%}$	$MC_{Goet\%}$
Northern Africa – Sahara	Tunisia	4.1	2.2	1.2	1.1
	Morocco	3.6	1.4	0.4	1.0
	Libya	5.2	3.1	0.9	2.2
	Algeria	6.6	2.7	1.4	1.4
	Mauritania	8.1	3.3	3.3	0.0

Sahel	Niger	6.1	5.8	2.3	3.5
	Mali	6.6	3.7	2.0	1.7
	Bodélé	4.1	0.7	0.7	0.0
Eastern Africa and the Middle East	Ethiopia	6.8	2.0	2.0	0.0
	Saudi Arabia	3.8	2.6	1.8	0.8
	Kuwait	5.0	1.5	1.5	0.0
Eastern Asia	Gobi	4.8	0.9	0.9	0.0
	Taklimakan	5.8	–	–	–
North America	Arizona	5.3	1.5	1.5	0.0
South America	Atacama	4.7	1.6	1.6	0.0
	Patagonia	5.1	1.5	0.9	0.6
Southern Africa	Namib—1	2.4	1.1	0.8	0.3
	Namib—2	10.6	4.8	4.8	0.0
Australia	Australia	7.2	3.6	3.6	0.0
Full dataset mean (st. dev.)		**5.6 (1.9)**	**2.4 (1.4)**	**1.8 (1.1)**	**0.7 (1.0)**

1292

Table 4. Real (n) and imaginary (k) parts of the refractive index estimated for the nineteen analysed dust samples and mean values calculated for the eight regions and for the full dataset. Data for single soils are reported as experiment–averaged values and their uncertainty is calculated as indicated in Table 1. Mean values and standard deviations at each wavelength based on single sample data are reported for the eight regions and the full dataset. The median and 10% and 90% percentile values are also reported for the full dataset. For North America and Australia, for which only one dust sample was analysed, the reported data correspond to the single sample available from these regions. For the real part, the average over the whole shortwave range (n_{SW}) is indicated.

Sample/Region	n_{SW} 037–0.95 µm	σ_{nSW} 037–0.95 µm	k 0.37 µm	k 0.47 µm	k 0.52 µm	k 0.59 µm	k 0.66 µm	k 0.88 µm	k 0.95 µm	σ_k 0.37 µm	σ_k 0.47 µm	σ_k 0.52 µm	σ_k 0.59 µm	σ_k 0.66 µm	σ_k 0.88 µm	σ_k 0.95 µm
Tunisia	1.51	0.06	0.0045	0.0035	0.0026	0.0018	0.0015	0.0013	0.0012	0.0030	0.0026	0.0018	0.0012	0.0010	0.0008	0.0007
Morocco	1.49	0.03	0.0023	0.0016	0.0012	0.0008	0.0007	0.0006	0.0007	0.0006	0.0004	0.0003	0.0002	0.0002	0.0002	0.0002
Lybia	1.5	0.04	0.0029	0.0019	0.0014	0.0007	0.0006	0.0007	0.0007	0.0006	0.0004	0.0002	0.0001	0.0002	0.0002	0.0002
Algeria	1.52	0.04	0.0025	0.0016	0.0012	0.0007	0.0005	0.0006	0.0006	0.0010	0.0006	0.0004	0.0003	0.0003	0.0003	0.0003
Mauritania	1.5	0.03	0.0043	0.0033	0.0026	0.0014	0.0013	0.0010	0.0010	0.0010	0.0009	0.0008	0.0003	0.0003	0.0004	0.0003
Northern Africa – Sahara (mean and st. dev.)	**1.51**	**0.03**	**0.0033**	**0.0024**	**0.0018**	**0.0011**	**0.0009**	**0.0008**	**0.0008**	**0.0010**	**0.0010**	**0.0007**	**0.0005**	**0.0004**	**0.0003**	**0.0003**
Niger	1.51	0.04	0.0088	0.0061	0.0048	0.0034	0.0031	0.0028	0.0021	0.0043	0.0031	0.0023	0.0018	0.0015	0.0010	0.0013
Mali	1.52	0.05	0.0048	0.0038	0.0030	0.0023	0.0024	0.0021	0.0021	0.0008	0.0006	0.0004	0.0003	0.0003	0.0003	0.0003
Bodélé	1.49	0.03	0.0011	0.0007	0.0006	0.0004	0.0004	0.0003	0.0003	0.0006	0.0004	0.0003	0.0002	0.0002	0.0001	0.0001
Sahel (mean and st. dev.)	**1.51**	**0.03**	**0.0049**	**0.0035**	**0.0028**	**0.0020**	**0.0020**	**0.0017**	**0.0015**	**0.0038**	**0.0027**	**0.0021**	**0.0015**	**0.0014**	**0.0013**	**0.0011**
Ethiopia	1.55	0.06	0.0026	0.0020	0.0016	0.0013	0.0011	0.0007	0.0006	0.0009	0.0008	0.0007	0.0005	0.0004	0.0002	0.0002
Saudi Arabia	1.54	0.06	0.0028	0.0021	0.0015	0.0007	0.0006	0.0006	0.0006	0.0006	0.0005	0.0004	0.0002	0.0001	0.0001	0.0001
Kuwait	1.50	0.04	0.0016	0.0010	0.0008	0.0006	0.0005	0.0005	0.0004	0.0005	0.0003	0.0003	0.0002	0.0002	0.0003	0.0002
Eastern Africa and the Middle East (mean and st. dev.)	**1.53**	**0.05**	**0.0023**	**0.0017**	**0.0013**	**0.0009**	**0.0007**	**0.0006**	**0.0005**	**0.0007**	**0.0006**	**0.0005**	**0.0004**	**0.0003**	**0.0001**	**0.0001**
Gobi	1.48	0.05	0.0041	0.0025	0.0018	0.0012	0.0011	0.0012	0.0012	0.0017	0.0009	0.0006	0.0004	0.0004	0.0005	0.0005
Taklimakan	1.54	0.07	0.0018	0.0012	0.0009	0.0006	0.0005	0.0005	0.0005	0.0008	0.0005	0.0004	0.0002	0.0002	0.0002	0.0002
Eastern Asia (mean and st. dev.)	**1.51**	**0.05**	**0.0030**	**0.0019**	**0.0014**	**0.0009**	**0.0008**	**0.0008**	**0.0009**	**0.0016**	**0.0009**	**0.0006**	**0.0005**	**0.0005**	**0.0005**	**0.0005**
Arizona	1.51	0.05	0.0011	0.0009	0.0007	0.0005	0.0005	0.0005	0.0004	0.0005	0.0004	0.0003	0.0002	0.0002	0.0002	0.0002
North America (mean and st. dev.)	**1.51**	**0.05**	**0.0011**	**0.0009**	**0.0007**	**0.0005**	**0.0005**	**0.0005**	**0.0004**	**0.0005**	**0.0004**	**0.0003**	**0.0002**	**0.0002**	**0.0002**	**0.0002**
Atacama	1.54	0.07	0.0016	0.0015	0.0012	0.0008	0.0006	0.0006	0.0006	0.0005	0.0004	0.0003	0.0002	0.0002	0.0002	0.0002
Patagonia	1.53	0.07	0.0024	0.0016	0.0011	0.0009	0.0006	0.0007	0.0006	0.0008	0.0005	0.0003	0.0003	0.0003	0.0003	0.0002
South America (mean and st. dev.)	**1.54**	**0.06**	**0.0020**	**0.0015**	**0.0011**	**0.0008**	**0.0006**	**0.0007**	**0.0006**	**0.0006**	**0.0001**	**0.0001**	**0.0001**	**0.0000**	**0.0001**	**0.0000**
Namib–1	1.53	0.06	0.0012	0.0009	0.0006	0.0004	0.0003	0.0004	0.0004	0.0006	0.0004	0.0003	0.0002	0.0001	0.0002	0.0001
Namib–2	1.55	0.07	0.0072	0.0054	0.0044	0.0025	0.0018	0.0014	0.0014	0.0027	0.0019	0.0016	0.0009	0.0007	0.0006	0.0006
Southern Africa (mean and st. dev.)	**1.54**	**0.06**	**0.0042**	**0.0031**	**0.0025**	**0.0014**	**0.0011**	**0.0009**	**0.0009**	**0.0042**	**0.0032**	**0.0027**	**0.0015**	**0.0010**	**0.0007**	**0.0007**
Australia	1.54	0.06	0.0058	0.0042	0.0033	0.0017	0.0013	0.0013	0.0012	0.0022	0.0011	0.0010	0.0006	0.0006	0.0004	0.0003
Australia (mean and st. dev.)	**1.54**	**0.06**	**0.0058**	**0.0042**	**0.0033**	**0.0017**	**0.0013**	**0.0013**	**0.0012**	**0.0022**	**0.0011**	**0.0010**	**0.0006**	**0.0006**	**0.0004**	**0.0003**
Full dataset (mean and st. dev.)	**1.52**	**0.04**	**0.0033**	**0.0024**	**0.0018**	**0.0012**	**0.0010**	**0.0009**	**0.0009**	**0.0021**	**0.0016**	**0.0013**	**0.0008**	**0.0007**	**0.0006**	**0.0005**
Full dataset median	**1.52**		**0.0026**	**0.0019**	**0.0014**	**0.0008**	**0.0006**	**0.0007**	**0.0006**							
Full dataset 10% percentile	**1.49**		**0.0012**	**0.0009**	**0.0007**	**0.0005**	**0.0004**	**0.0004**	**0.0004**							

| Full dataset 90% percentile | 1.54 | | | 0.00 61 | 0.00 44 | 0.00 35 | 0.00 23 | 0.00 19 | 0.00 15 | 0.00 15 | | | | | | | |

1302

Table 5. As in Table 4 for the single scattering albedo (SSA) data.

Sample/Region	SSA							σ_{SSA}						
	0.37 µm	0.47 µm	0.52 µm	0.59 µm	0.66 µm	0.88 µm	0.95 µm	0.37 µm	0.47 µm	0.52 µm	0.59 µm	0.66 µm	0.88 µm	0.95 µm
Tunisia	0.85	0.90	0.93	0.95	0.95	0.97	0.97	0.03	0.02	0.02	0.01	0.01	0.01	0.01
Morocco	0.92	0.95	0.96	0.98	0.98	0.98	0.99	0.01	0.01	0.01	0.00	0.00	0.00	0.00
Lybia	0.89	0.93	0.95	0.98	0.98	0.98	0.98	0.02	0.01	0.01	0.00	0.00	0.00	0.00
Algeria	0.87	0.92	0.94	0.97	0.97	0.98	0.98	0.02	0.01	0.01	0.00	0.00	0.00	0.00
Mauritania	0.85	0.90	0.94	0.96	0.97	0.98	0.98	0.02	0.01	0.01	0.01	0.01	0.00	0.00
Northern Africa – Sahara (mean and st. dev.)	**0.88**	**0.92**	**0.94**	**0.97**	**0.97**	**0.98**	**0.98**	**0.03**	**0.02**	**0.02**	**0.01**	**0.01**	**0.01**	**0.01**
Niger	0.72	0.85	0.89	0.91	0.92	0.94	0.95	0.09	0.09	0.07	0.05	0.05	0.03	0.02
Mali	0.75	0.85	0.89	0.93	0.95	0.96	0.96	0.04	0.03	0.02	0.02	0.02	0.01	0.01
Bodélé	0.96	0.98	0.98	0.99	0.99	0.99	0.99	0.04	0.02	0.02	0.01	0.01	0.01	0.01
Sahel (mean and st. dev.)	**0.81**	**0.89**	**0.92**	**0.94**	**0.95**	**0.96**	**0.97**	**0.13**	**0.07**	**0.05**	**0.04**	**0.04**	**0.03**	**0.02**
Ethiopia	0.80	0.86	0.90	0.92	0.94	0.97	0.97	0.03	0.03	0.02	0.02	0.01	0.01	0.01
Saudi Arabia	0.88	0.93	0.96	0.98	0.98	0.98	0.98	0.03	0.02	0.01	0.01	0.01	0.00	0.00
Kuwait	0.95	0.97	0.98	0.98	0.99	0.99	0.99	0.02	0.01	0.01	0.01	0.01	0.01	0.00
Eastern Africa and the Middle East (mean and st. dev.)	**0.88**	**0.92**	**0.94**	**0.96**	**0.97**	**0.98**	**0.98**	**0.07**	**0.05**	**0.04**	**0.03**	**0.03**	**0.01**	**0.01**
Gobi	0.88	0.92	0.94	0.96	0.97	0.97	0.97	0.04	0.03	0.02	0.01	0.01	0.01	0.01
Taklimakan	0.82	0.88	0.92	0.95	0.96	0.96	0.96	0.03	0.02	0.02	0.01	0.01	0.01	0.01
Eastern Asia (mean and st. dev.)	**0.85**	**0.90**	**0.93**	**0.96**	**0.96**	**0.97**	**0.97**	**0.04**	**0.03**	**0.02**	**0.01**	**0.01**	**0.01**	**0.01**
Arizona	0.93	0.96	0.97	0.98	0.98	0.99	0.99	0.01	0.01	0.01	0.00	0.00	0.00	0.00
North America (mean and st. dev.)	**0.93**	**0.96**	**0.97**	**0.98**	**0.98**	**0.99**	**0.99**	**0.01**	**0.01**	**0.01**	**0.00**	**0.00**	**0.00**	**0.00**
Atacama	0.89	0.93	0.94	0.97	0.97	0.98	0.98	0.03	0.02	0.02	0.01	0.01	0.01	0.01
Patagonia	0.88	0.91	0.94	0.96	0.97	0.98	0.98	0.02	0.02	0.01	0.01	0.01	0.00	0.01
South America (mean and st. dev.)	**0.89**	**0.92**	**0.94**	**0.96**	**0.97**	**0.98**	**0.98**	**0.00**	**0.01**	**0.00**	**0.00**	**0.00**	**0.00**	**0.00**
Namib-–1	0.91	0.95	0.96	0.98	0.98	0.99	0.99	0.02	0.01	0.01	0.00	0.00	0.00	0.00
Namib-–2	0.74	0.82	0.86	0.92	0.94	0.96	0.97	0.03	0.02	0.02	0.01	0.01	0.01	0.01
Southern Africa (mean and st. dev.)	**0.83**	**0.88**	**0.91**	**0.95**	**0.96**	**0.98**	**0.98**	**0.12**	**0.09**	**0.07**	**0.04**	**0.03**	**0.02**	**0.02**
Australia	0.70	0.81	0.85	0.91	0.93	0.96	0.97	0.04	0.03	0.02	0.01	0.01	0.01	0.01
Australia (mean and st. dev.)	**0.70**	**0.81**	**0.85**	**0.91**	**0.93**	**0.96**	**0.97**	**0.04**	**0.03**	**0.02**	**0.01**	**0.01**	**0.01**	**0.01**
Full dataset (mean and st. dev.)	**0.85**	**0.91**	**0.93**	**0.96**	**0.96**	**0.97**	**0.98**	**0.08**	**0.05**	**0.04**	**0.03**	**0.02**	**0.01**	**0.01**
Full dataset median	**0.88**	**0.92**	**0.94**	**0.96**	**0.97**	**0.98**	**0.98**							
Full dataset 10% percentile	**0.74**	**0.84**	**0.88**	**0.92**	**0.94**	**0.96**	**0.96**							
Full dataset 90% percentile	**0.93**	**0.96**	**0.97**	**0.98**	**0.99**	**0.99**	**0.99**							

1304

Table 6. Results of the linear fit between k and SSA and the mass concentration of iron oxides, $MC_{Fe-ox\%}$, hematite, $MC_{Hem\%}$, goethite, $MC_{Goeth\%}$, and elemental iron, $MC_{Fe\%}$ in dust. Column 1 indicates the wavelength; (a ± σa) indicates the retrieved slope and its estimated uncertainty; (b ± σb) indicates the retrieved intercept and its estimated uncertainty; R^2 denotes the correlation coefficient and χ^2_{red} is the reduced chi–square of the fit.

	$k = a\,MC_{Fe-ox\,\%} + b$			$SSA = a\,MC_{Fe-ox\,\%} + b$		
Wavelength (nm)	$a \pm \sigma a$	$b \pm \sigma b$	R^2 ; χ^2_{red}	$a \pm \sigma a$	$b \pm \sigma b$	R^2 ; χ^2_{red}
370	$(11.9 \pm 2.4)\,10^{-4}$	$(2.4 \pm 4.6)\,10^{-4}$	0.88 ; 0.6	$(-5.8 \pm 0.8)\,10^{-2}$	(1.00 ± 0.02)	0.83 ; 1.7
470	$(9.0 \pm 1.7)\,10^{-4}$	$(1.7 \pm 3.2)\,10^{-4}$	0.89 ; 0.8	$(-3.8 \pm 0.6)\,10^{-2}$	(1.00 ± 0.01)	0.78 ; 1.8
520	$(6.8 \pm 1.3)\,10^{-4}$	$(1.3 \pm 2.4)\,10^{-4}$	0.90 ; 0.9	$(-2.9 \pm 0.4)\,10^{-2}$	(1.01 ± 0.01)	0.76 ; 2.0
590	$(4.5 \pm 0.9)\,10^{-4}$	$(0.9 \pm 1.6)\,10^{-4}$	0.85 ; 1.4	$(-1.8 \pm 0.3)\,10^{-2}$	(1.00 ± 0.01)	0.75 ; 2.3
660	$(4.3 \pm 0.8)\,10^{-4}$	$(0.8 \pm 1.4)\,10^{-4}$	0.81 ; 1.6	$(-1.3 \pm 0.2)\,10^{-2}$	(1.00 ± 0.00)	0.75 ; 2.2
880	$(3.4 \pm 0.6)\,10^{-4}$	$(0.6 \pm 1.2)\,10^{-4}$	0.79 ; 1.0	$(-0.76 \pm 0.16)\,10^{-2}$	(1.00 ± 0.00)	0.79 ; 1.4
950	$(3.2 \pm 0.6)\,10^{-4}$	$(0.6 \pm 1.0)\,10^{-4}$	0.77 ; 1.1	$(-0.62 \pm 0.13)\,10^{-2}$	(0.99 ± 0.00)	0.78 ; 1.1
	$k = a\,MC_{Hem\,\%} + b$			$SSA = a\,MC_{Hem\,\%} + b$		
Wavelength (nm)	$a \pm \sigma a$	$b \pm \sigma b$	R^2 ; χ^2_{red}	$a \pm \sigma a$	$b \pm \sigma b$	R^2 ; χ^2_{red}
370	$(9.7 \pm 2.7)\,10^{-4}$	$(2.7 \pm 4.0)\,10^{-4}$	0.67 ; 1.9	$(-4.4 \pm 0.6)\,10^{-2}$	(0.95 ± 0.01)	0.73 ; 3.5
470	$(8.3 \pm 1.9)\,10^{-4}$	$(1.9 \pm 2.7)\,10^{-4}$	0.72 ; 1.9	$(-3.0 \pm 0.4)\,10^{-2}$	(0.97 ± 0.01)	0.76 ; 3.2
520	$(6.9 \pm 1.5)\,10^{-4}$	$(1.5 \pm 2.0)\,10^{-4}$	0.74 ; 2.0	$(-2.2 \pm 0.3)\,10^{-2}$	(0.98 ± 0.00)	0.78 ; 3.3
590	$(3.7 \pm 0.8)\,10^{-4}$	$(0.9 \pm 1.2)\,10^{-4}$	0.61 ; 2.1	$(-1.3 \pm 0.2)\,10^{-2}$	(0.99 ± 0.00)	0.71 ; 2.7
660	$(3.7 \pm 0.8)\,10^{-4}$	$(0.8 \pm 1.1)\,10^{-4}$	0.51 ; 2.6	$(-0.9 \pm 0.2)\,10^{-2}$	(0.99 ± 0.00)	0.62 ; 2.5
880	$(2.9 \pm 0.7)\,10^{-4}$	$(0.7 \pm 1.1)\,10^{-4}$	0.43 ; 2.1	$(-0.6 \pm 0.1)\,10^{-2}$	(0.99 ± 0.00)	0.57 ; 1.8
950	$(2.6 \pm 0.6)\,10^{-4}$	$(0.6 \pm 0.9)\,10^{-4}$	0.46 ; 2.1	$(-0.5 \pm 0.1)\,10^{-2}$	(0.99 ± 0.00)	0.49 ; 1.7
	$k = a\,MC_{Goeth\,\%} + b$			$SSA = a\,MC_{Goeth\,\%} + b$		
Wavelength (nm)	$a \pm \sigma a$	$b \pm \sigma b$	R^2 ; χ^2_{red}	$a \pm \sigma a$	$b \pm \sigma b$	R^2 ; χ^2_{red}
370	$(9.0 \pm 2.5)\,10^{-4}$	$(2.5 \pm 2.2)\,10^{-4}$	0.47 ; 1.8	$(-13.4 \pm 6.9)\,10^{-3}$	(0.90 ± 0.01)	0.32 ; 6.8
470	$(5.5 \pm 1.7)\,10^{-4}$	$(1.7 \pm 1.5)\,10^{-4}$	0.43 ; 2.3	$(-8.3 \pm 4.7)\,10^{-3}$	(0.94 ± 0.00)	0.21 ; 6.2
520	$(3.4 \pm 1.1)\,10^{-4}$	$(1.1 \pm 1.2)\,10^{-4}$	0.41 ; 2.5	$(-4.9 \pm 3.2)\,10^{-3}$	(0.96 ± 0.00)	0.17 ; 6.4
590	$(0.5 \pm 0.6)\,10^{-4}$	$(0.6 \pm 0.8)\,10^{-4}$	0.50 ; 3.2	$(0.9 \pm 2.0)\,10^{-3}$	(0.97 ± 0.00)	0.23 ; 5.5
660	$(2.2 \pm 0.8)\,10^{-4}$	$(0.8 \pm 0.7)\,10^{-4}$	0.55 ; 3.6	$(0.2 \pm 1.6)\,10^{-3}$	(0.98 ± 0.00)	0.34 ; 4.4
880	$(2.6 \pm 0.8)\,10^{-4}$	$(0.8 \pm 0.6)\,10^{-4}$	0.62 ; 2.4	$(-1.1 \pm 1.4)\,10^{-3}$	(0.98 ± 0.00)	0.47 ; 3.0
950	$(2.6 \pm 0.8)\,10^{-4}$	$(0.8 \pm 0.6)\,10^{-4}$	0.55 ; 2.5	$(-2.1 \pm 1.4)\,10^{-3}$	(0.98 ± 0.00)	0.54 ; 2.6
	$k = a\,MC_{Fe\,\%} + b$			$SSA = a\,MC_{Fe\,\%} + b$		
Wavelength (nm)	$a \pm \sigma a$	$b \pm \sigma b$	R^2 ; χ^2_{red}	$a \pm \sigma a$	$b \pm \sigma b$	R^2 ; χ^2_{red}
370	$(6.0 \pm 1.4)\,10^{-4}$	$(1.4 \pm 0.7)\,10^{-4}$	0.60 ; 1.5	$(-2.7 \pm 0.4)\,10^{-2}$	(1.02 ± 0.02)	0.67 ; 3.1
470	$(4.7 \pm 1.0)\,10^{-4}$	$(1.0 \pm 0.5)\,10^{-4}$	0.62 ; 1.7	$(-1.8 \pm 0.3)\,10^{-2}$	(1.02 ± 0.01)	0.72 ; 2.8
520	$(3.9 \pm 0.8)\,10^{-4}$	$(0.8 \pm 3.9)\,10^{-4}$	0.65 ; 1.6	$(-1.3 \pm 0.2)\,10^{-2}$	(1.01 ± 0.01)	0.72 ; 2.9
590	$(2.5 \pm 0.5)\,10^{-4}$	$(0.5 \pm 2.4)\,10^{-4}$	0.56 ; 1.7	$(-0.8 \pm 0.1)\,10^{-2}$	(1.01 ± 0.01)	0.70 ; 2.4
660	$(2.0 \pm 0.4)\,10^{-4}$	$(0.4 \pm 1.7)\,10^{-4}$	0.48 ; 1.9	$(-0.5 \pm 0.1)\,10^{-2}$	(1.00 ± 0.00)	0.62 ; 2.0
880	$(1.8 \pm 0.4)\,10^{-4}$	$(0.4 \pm 2.0)\,10^{-4}$	0.40 ; 1.8	$(-0.4 \pm 0.1)\,10^{-2}$	(1.00 ± 0.00)	0.54 ; 1.6

| 950 | $(1.4 \pm 0.3)\ 10^{-4}$ | $(0.3 \pm 1.4)\ 10^{-4}$ | 0.45 ; 2.0 | $(-0.3 \pm 0.1)\ 10^{-2}$ | (1.00 ± 0.00) | 0.49 ; 1.5 |

Figure 1. Flowchart illustrating the procedure for data treatment and retrieval of physical and chemical (size, composition) and spectral optical properties (single scattering albedo, SSA, and complex refractive index) of mineral dust aerosols. In red we mention the different corrections performed and the values adopted in the calculations.
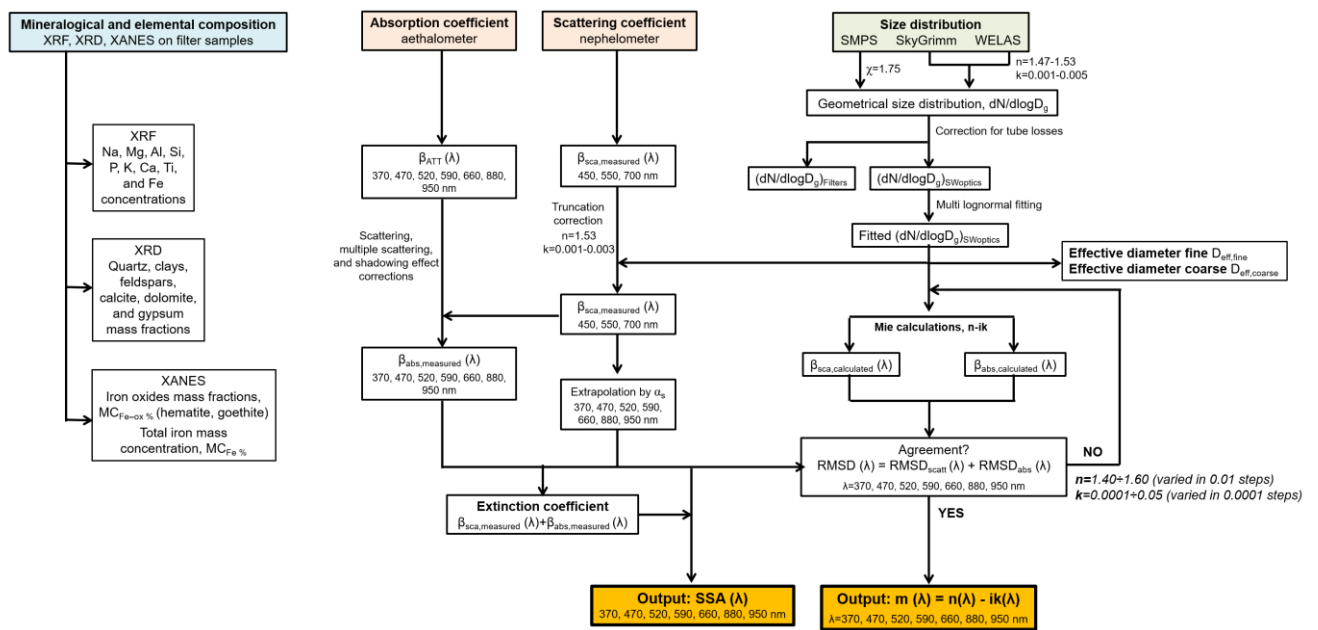
1326
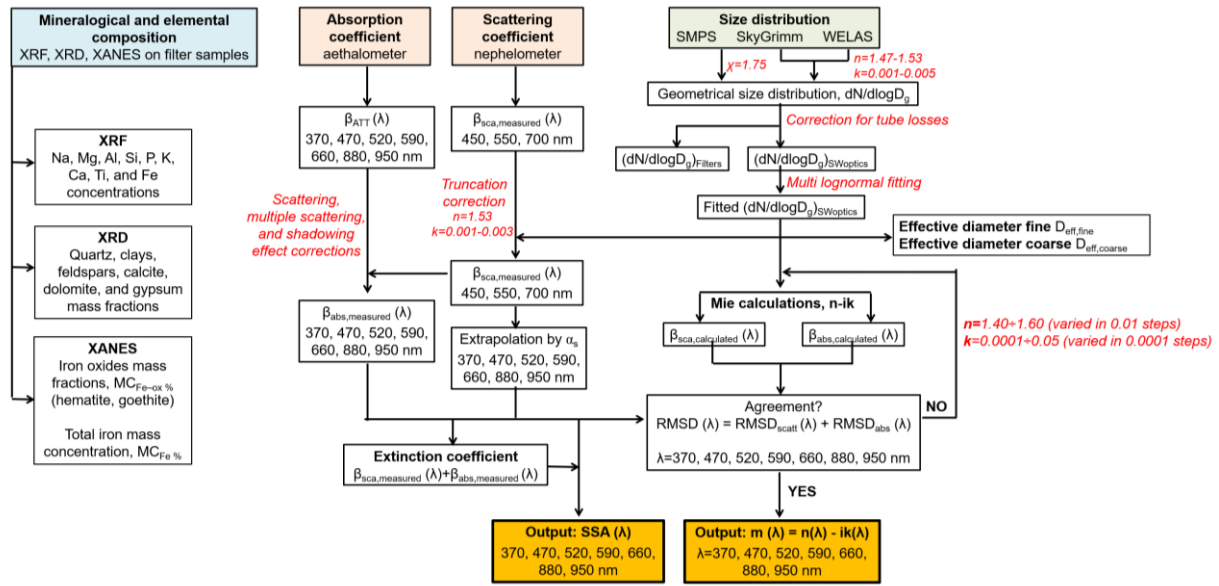
1327
1328
1329 **Figure 2.** Box and whisker plot showing the full variability of hematite and goethite mass fractions in
1330 the soils for the clay–sized (<2 µm diameter) and silt–sized (<60 µm diameter) soil fractions as retrieved
1331 from the global soil mineralogical database by Journet et al. (2014). The box and whisker plot include
1332 data for the nineData are desert source areas depicted in Ginoux et al. (2012) and DB17 (Northern
1333 Africa, Sahel, Eastern Africa and the Middle East, Central Asia, Eastern Asia, North America, South
1334 America, Southern Africa, and Australia). from the soil mineralogical database by Journet et al. (2014).
1335 in the dust source regions at the global scale by considering desert source areas as reported in Ginoux
1336 et al. (2012) and DB17. Data are from the soil mineralogical database by Journet et al. (2014). Dots
1337 indicate hematite and goethite soil content in clay–sized and silt–sized soils (always extracted from
1338 Journet et al.) extracted in correspondence to the geographical coordinates where thefor the nineteen
1339 soils used in the CESAM experiments were collected. The Journet et al. database assumes that the
1340 iron oxides in the silt fraction consist only of goethite.
1341
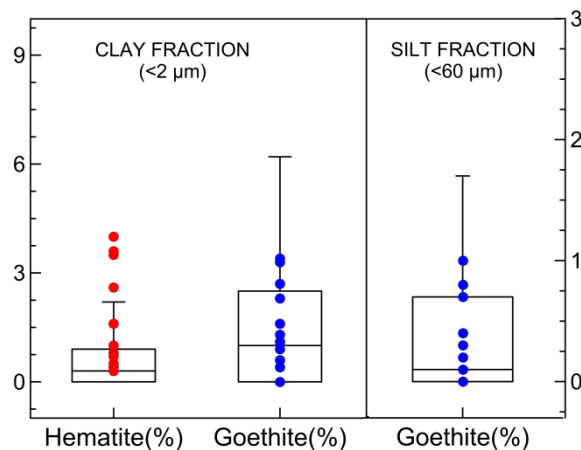
1342
1343
1344
1345

1346 **Figure 3.** Top panel: time series of the aerosol mass concentration (cross symbols) and effective fine

1347 ($D_{eff,fine}$, open dots) and coarse diameter ($D_{eff,coarse}$, open squares) measured inside the CESAM cham-

1348 ber (red symbols) and at the input of the SW instruments (black symbols) for one experiment (Morocco

1349 dust). Bottom panel: time series of the scattering β_{sca} and absorption β_{abs} coefficients at 370 nm for the

1350 same experiment. Mass concentrations are reported as 6-–sec data, while all other quantities are 10–

1351 min averages.
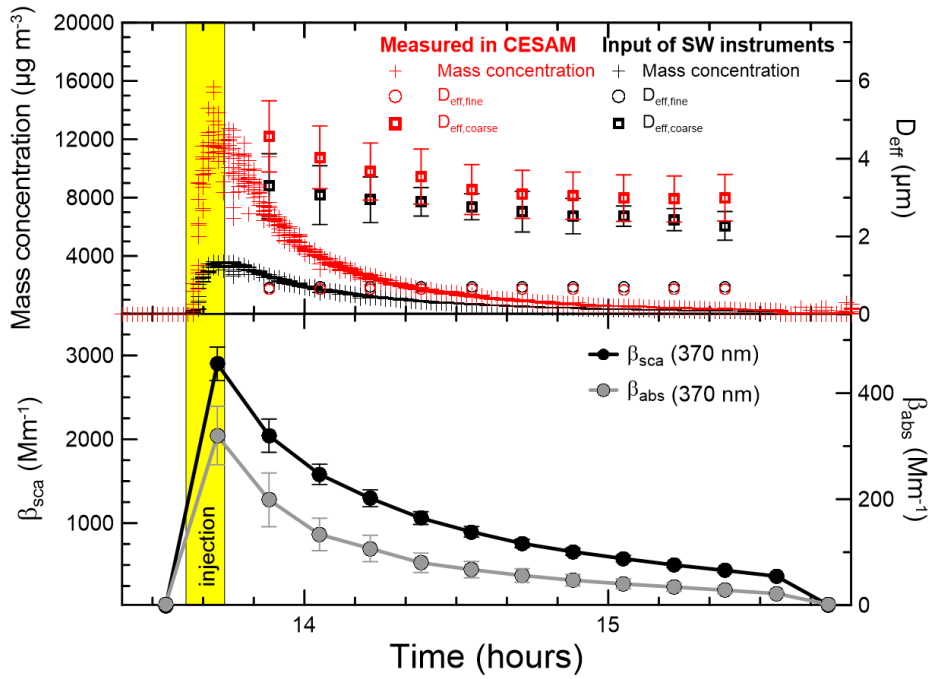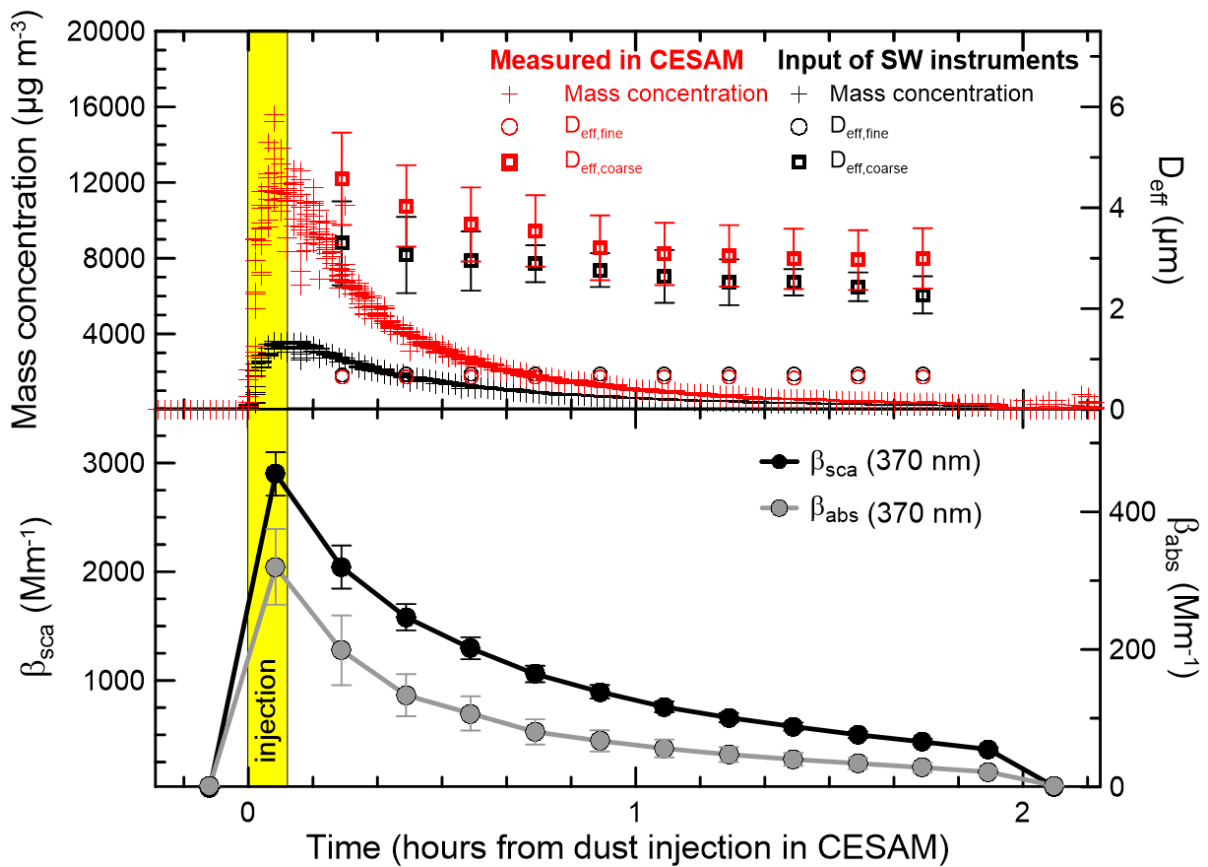
1359
1360
1361
1362
1363
1364
1365
1366
1367
1368
1369
1370
1371

Figure 4. Comparison of dust size distributions sensed by the SW optical instruments (behind the SW instruments inlet $(dV/dlogD_g)_{SWoptics}$), with field data for long–range transported dust. The thick black line represents the mean value of $(dV/dlogD_g)_{SWoptics}$ at the peak of the dust injection in CESAM for experiments with the different samples. The grey shaded area indicates the range of $(dV/dlogD_g)_{SWoptics}$ for all samples. The dotted black line shows the average of the dust size distribution at the peak of the injection inside the CESAM chamber from DB17. Field data are from: Formenti et al. (2001) (CLAIRE campaign in Suriname, South America), Maring et al. (2003) and Denjean et al. (2016b) (PRIDE and DUST– ATTACK campaigns in Puerto Rico, Caraibes), Müller et al. (2011), and Chen et al. (2011) and (Ryder et al. (2018) (SAMUM2, and NAMMA, and AER–D campaigns in Cape Verde, eastern Atlantic), and Weinzierl et al. (2017) (SALTRACE campaign, data from Barbados). For comparison, data taken close to the source in Niger from Formenti et al. (2011) during the AMMA campaign are also shown. SAL stands for Saharan Air Layer. All data are reported as volume size distributions normalised at the maximum.
(The different acronyms spell out as: AER–D= AERosol Properties – Dust; AMMA = African Monsoon Multidisciplinary Analysis; CLARE= Cooperative LBA Airborne Regional Experiment; DUST–ATTACK+ Dust Aging and TransporT from Africa to the Caribbean; NAMMA = NASA African Monsoon Multidisciplinary Analysis; PRIDE = Puerto Rico Dust Experiment; SALTRACE= Saharan Aerosol Long–range Transport and Aerosol–Cloud–Interaction Experiment; SAMUM = Saharan Mineral Dust Experiment).

1390
1391
1392

1393

1394
1395
1396
1397
1398
1399
1400
1401
1402
1403
1404

43
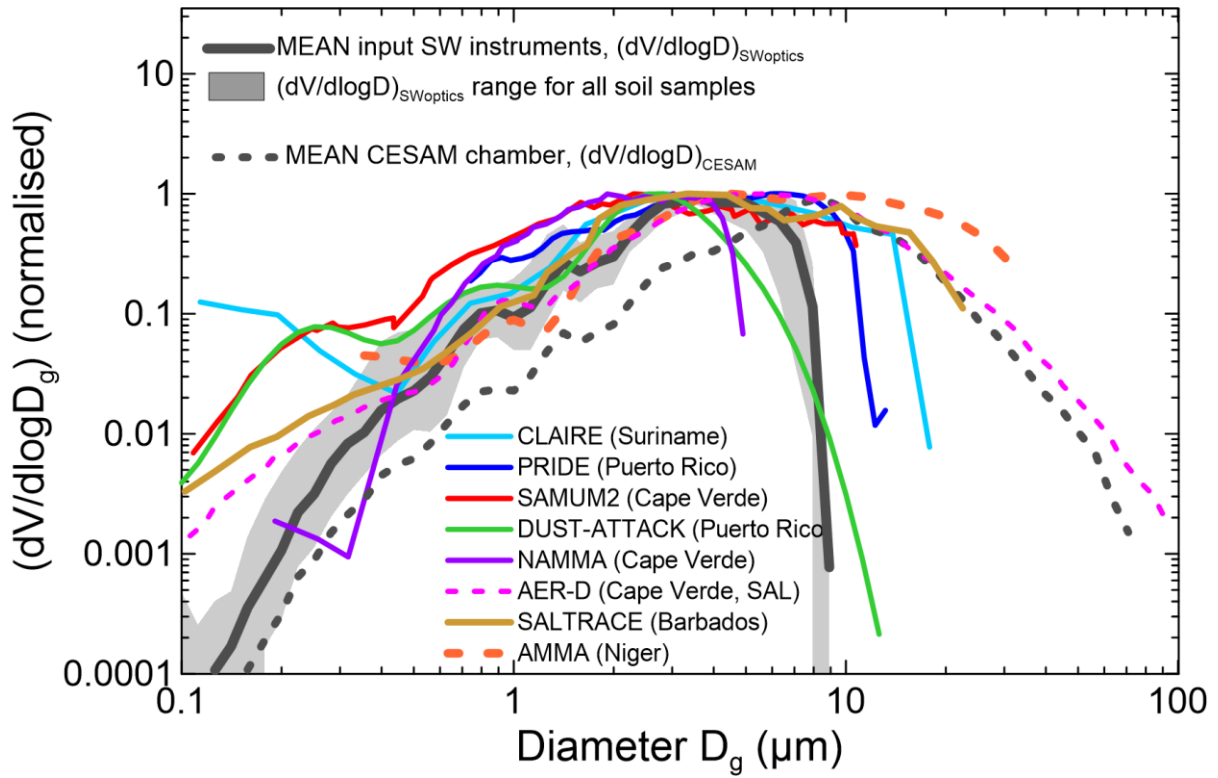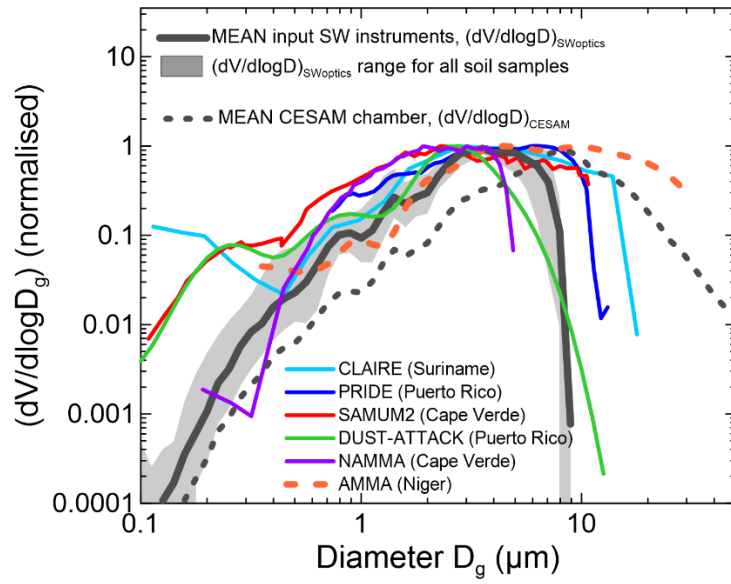
1405

1406

1407

1408

1409

1410

1411 **Figure 5.** Spectral extinction coefficient, absorption coefficient, SSA, and real (n) and imaginary (k)

1412 parts of the refractive index at the peak of the dust injection in the chamber and after 30 and 90 minutes

1413 for Morocco and Algeria dust samples. Data are reported at the seven aethalometer wavelengths (370,

1414 470, 520, 590, 660, 880, and 950 nm) as 10–min averages. In the top panel we report the extinction

1415 calculated as the sum of scattering and absorption coefficients. For the sake of clarity error bars are not

1416 shown for SSA, n, and k data.

1417
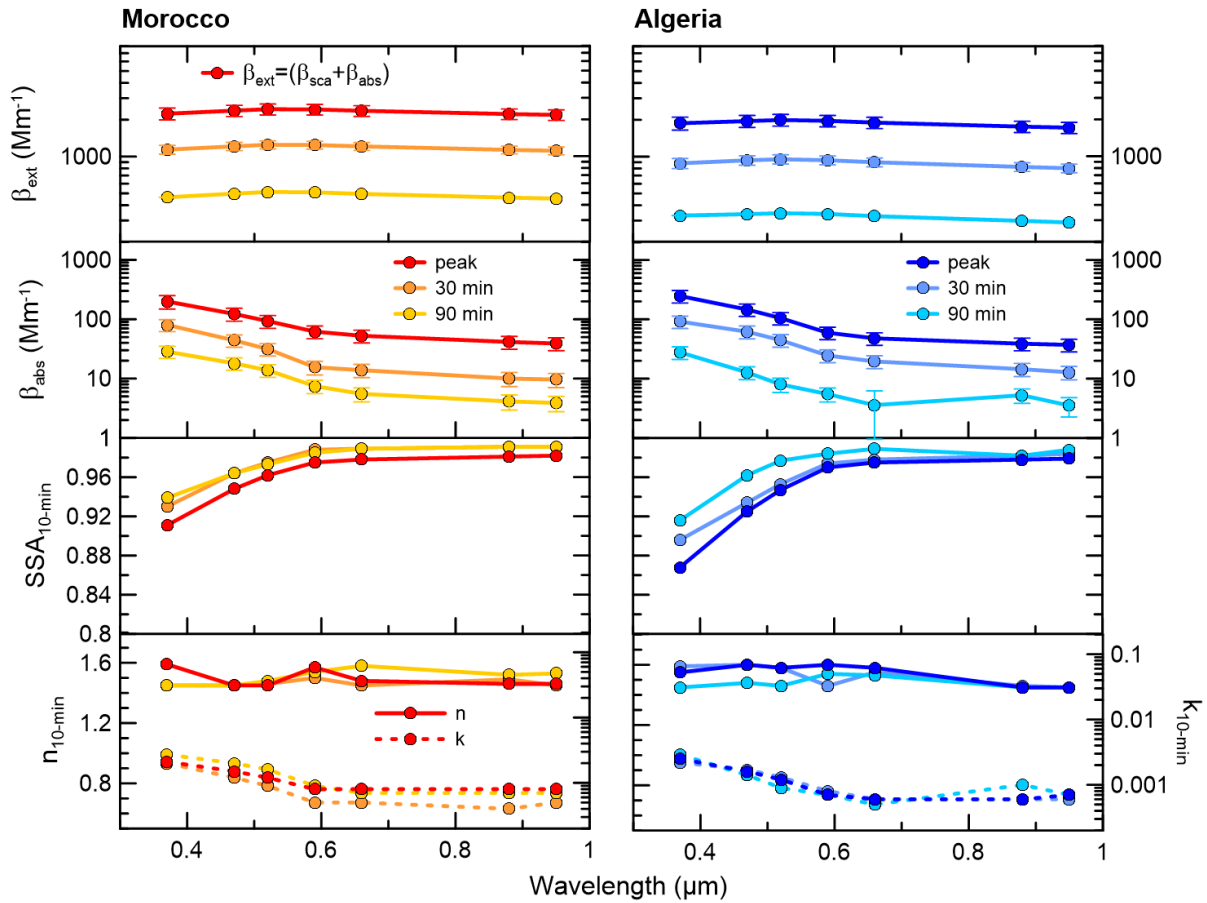
1418

1419

1420

1421

1422

1423

1424

1425

1426

1427

1428

1429

1430

1431

**Figure 6.** ~~(a)~~ Real (n) and imaginary (k) parts of the dust complex refractive index ~~and (b) single scattering albedo (SSA_AVG)~~ at seven wavelengths between 370 and 950 nm obtained for the 19 aerosol samples analyzed in this study. Data ~~for the refractive index~~ correspond to the time average of the 10 min values obtained between the peak of the injection and 120 min later. The error bar corresponds to the absolute uncertainty in n and k, estimated to be <8% for n and between 13 and 75 % for k. ~~SSA_AVG data correspond to the fit of the 10 min values of β_{sca} versus β_{abs}, and the uncertainty is between 1% and 12% at 370 nm and between 1% and 3% at 950 nm.~~

1439

1441

1442

1443

Figure 7. Single scattering albedo (SSA) at seven wavelengths between 370 and 950 nm obtained for the 19 aerosol samples analyzed in this study. Data correspond for each sample (with the exception of Tunisia and Namib–2, see Sect. 3.1) to the fit of the 10 min values of β_{sca} versus β_{abs}, and the uncertainty is between 1% and 12% at 370 nm and between 1% and 3% at 950 nm.
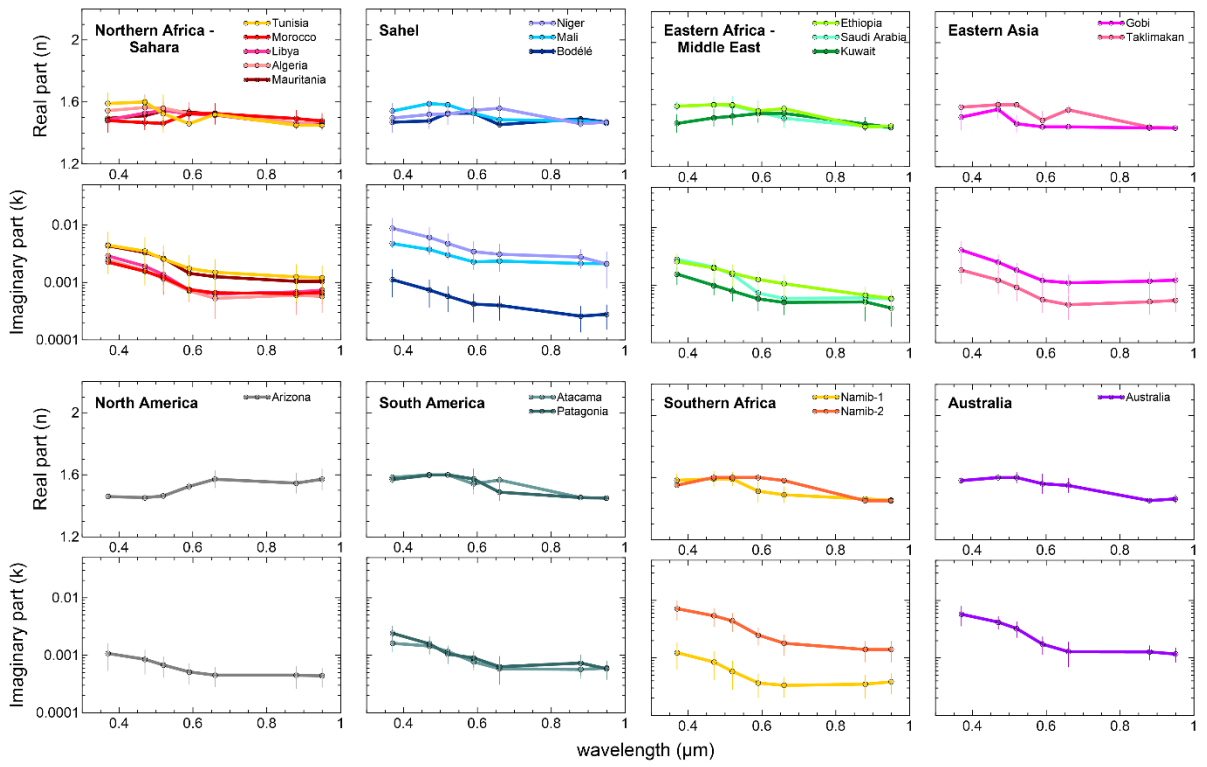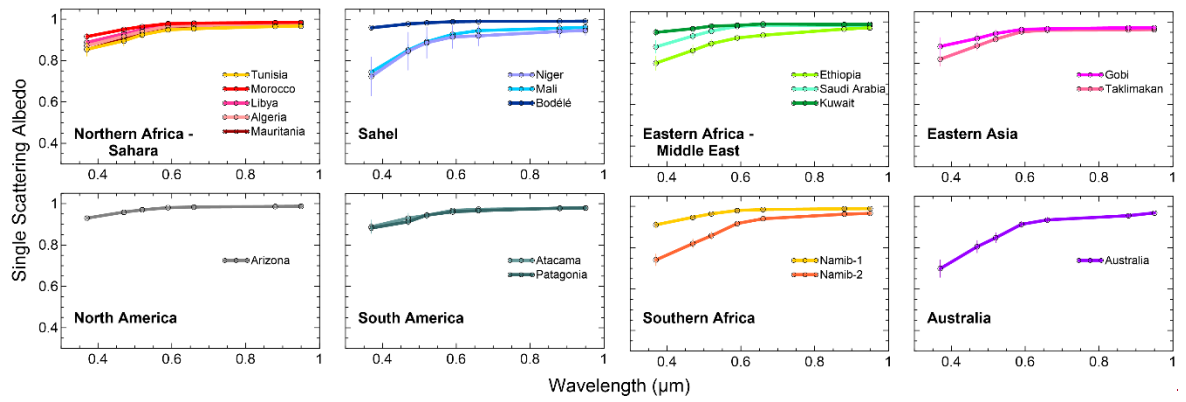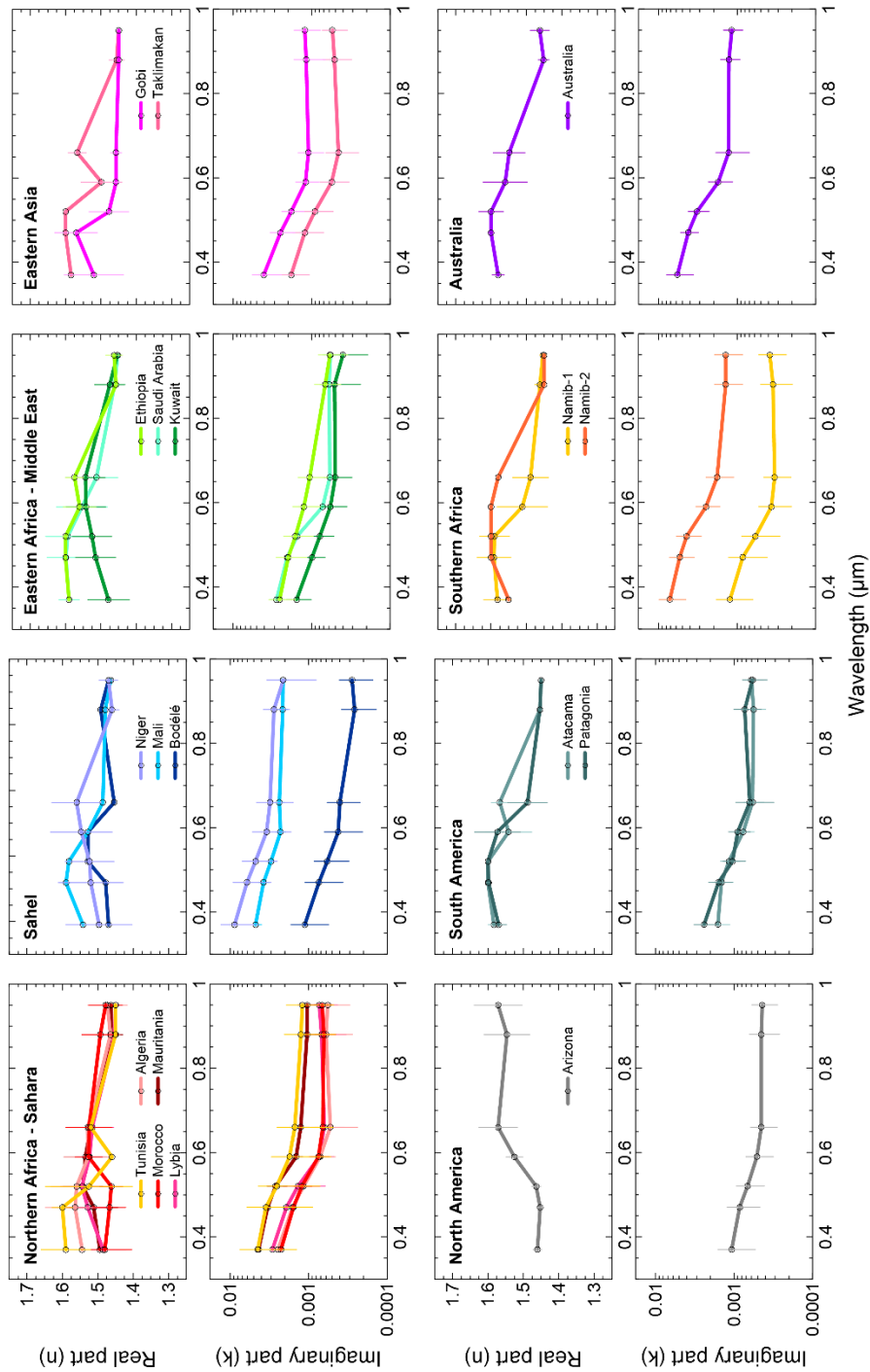
1444

1445

1446

1447

1448
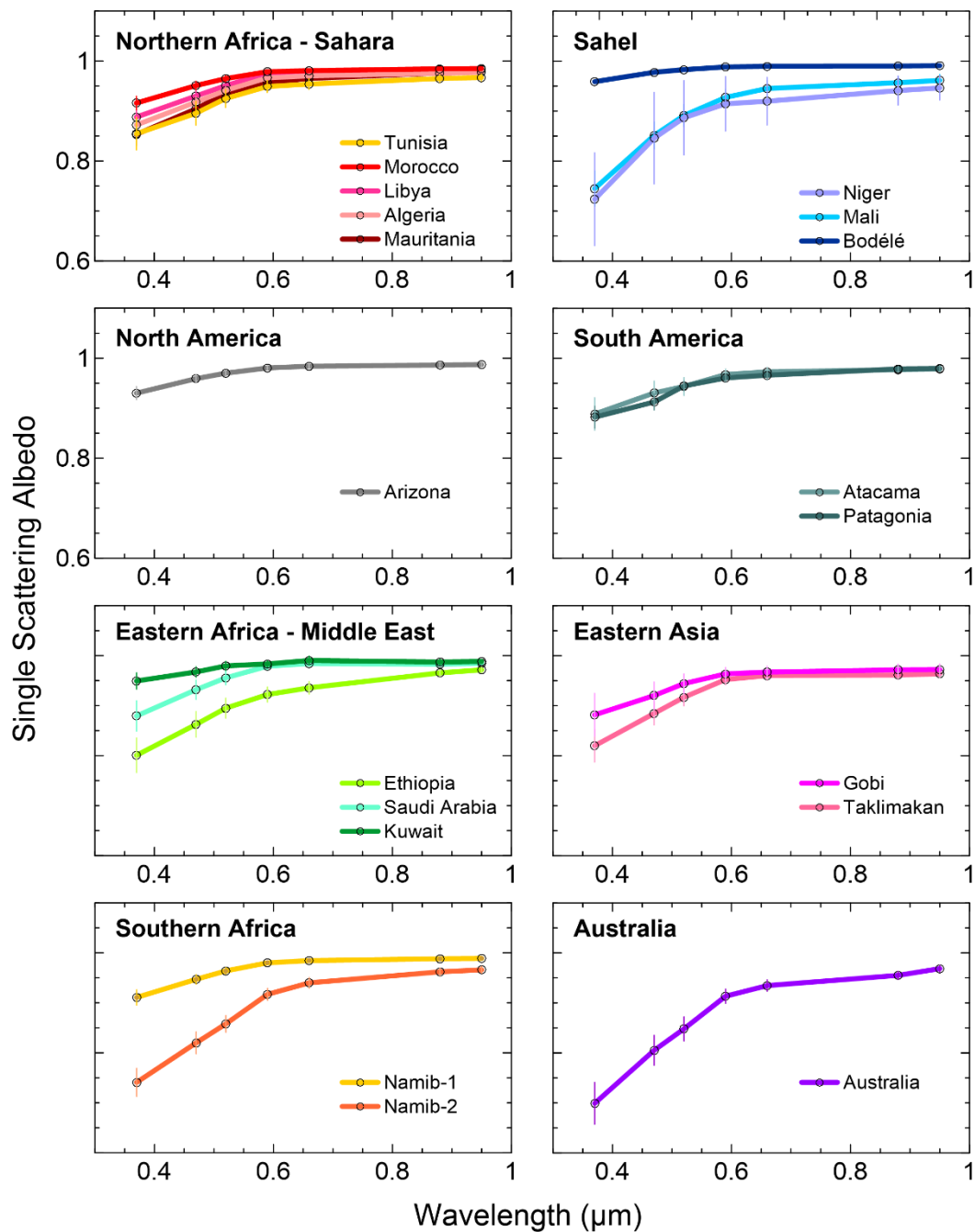
Figure 87. Comparison of results obtained in this study (a) with literature–compiled values (b) of the (a) dust real and imaginary parts of the refractive index (n, k) and (b) single scattering albedo (SSA) in the SW spectral range. The regions in graygrey in panel a) indicate the full range of variability obtained in this study, and the grayblack thick lines are the means of n, k and SSA obtained for the different aerosol samples. Literature values in panel b) include estimates from ground-based and aircraft observations

during field campaigns, laboratory studies, AERONET inversions, and estimates from dust mineralogical composition. Data are in some cases for the full dust size distribution, while in other only the fine fraction below about 2 μm is ~~measured~~ represented (identified with *).

The main provenance of the dust and datasets from the literature is provided in the following: Volz et al. (1972) is data for rainout dust collected in Germany; Patterson et al. (1977) is Saharan dust; Hess et al. (1998) is data from the OPAC database; Colarco et al. (2002) is data for dust from Dakar, Sal, and Tenerife; Dubovik et al. (2002) included data from Bahrain—Persian Gulf and Solar Village—Saudi Arabia AERONET stations; Haywood et al. (2003) is dust from Mauritania; Sinyuk et al. (2003) is data from Cape Verde, Dakar, and Burkina Faso; Clarke et al. (2004) is Asian dust offshore of China, Japan, and Korea; Linke et al. (2006)—A is dust from Cairo; Linke et al. (2006)—B is dust from Morocco; Balkanski et al (2007) is calculated from mineralogical composition assuming a 1.5% hematite mass fraction in dust; Todd et al. (2007) is from Bodélé; Osborne et al. (2008) is from Niger; Otto et al. (2009), Petzold et al. (2009), Schladitz et al. (2009), and Muller et al. (2010, 2011) is dust originated mostly in Morocco; McConnell et al. (2008, 2010) is dust from Niger/Senegal; Chen et al. (2011) is dust from Western Sahara; Formenti et al. (2011) in the k plot is an average of airborne observations for the AMMA campaign in Niger, while for the SSA plot, Formenti et al. (2011)—A is from observations in the Saharan Air Layer, —B is from Bodélé/Sudan, and –C is a Sahelian uplift episode; Johnson et al. (2011) is dust from Western Sahara; Moosmüller et al. (2012) analysed samples from Middle East, Mali and Spain, and here we report the average of their obtained values; Wagner et al. (2012) obtained k values for several samples from ~~Cairo and~~ Burkina Fas~~o,u~~ Cairo and the SAMUM campaign and here we report ~~and~~ the values for the maximum of their spectral k ~~average of its results~~ (Burkina Faso) and the minimum (Cairo); Ryder et al. (2013) is dust from Western Sahara and Mauritania and we report in both k and SSA plots the average of their observations; Engelbrecht et al. (2016) analysed many dust samples from all over the world, here we report their ~~measured~~ estimated minimum and maximum of the dust SSA that are –A from California and –B from the Etosha Pan in Namibia; Steigmann and Yang (2017) modelled the refractive index of dust based on assumed mineralogical compositions typical for Northern and Southern Sahara and Western and Eastern Asia dust, and here we report the average of their results for both n and k. Uncertainties in the field observations have been omitted for the sake of clarity. The legend identifies the line styles used in the plots.

(The different acronyms spell out as (see also the caption of Fig. 4): AERONET = Aerosol Robotic Network; OPAC = Optical Properties of Aerosols and Clouds; SHADE = Saharan Dust Experiment; BODEX = The Bodélé Dust Experiment; DABEX = Dust and Biomass Experiment; SAMUM1 and SAMUM2 refers to the two SAMUM campaigns in Morocco and Cape Verde, respectively, SAMUM = Saharan Mineral Dust Experiment; DODO = Dust Outflow and Deposition to the Ocean; ~~AMMA = African Monsoon Multidisciplinary Analysis; NAMMA = NASA African Monsoon Multidisciplinary Analysis;~~ ACE—Asia = Asian Pacific Regional Aerosol Characterization Experiment; GERBILS = Geostationary Earth Radiation Budget Intercomparison of Longwave and Shortwave radiation).
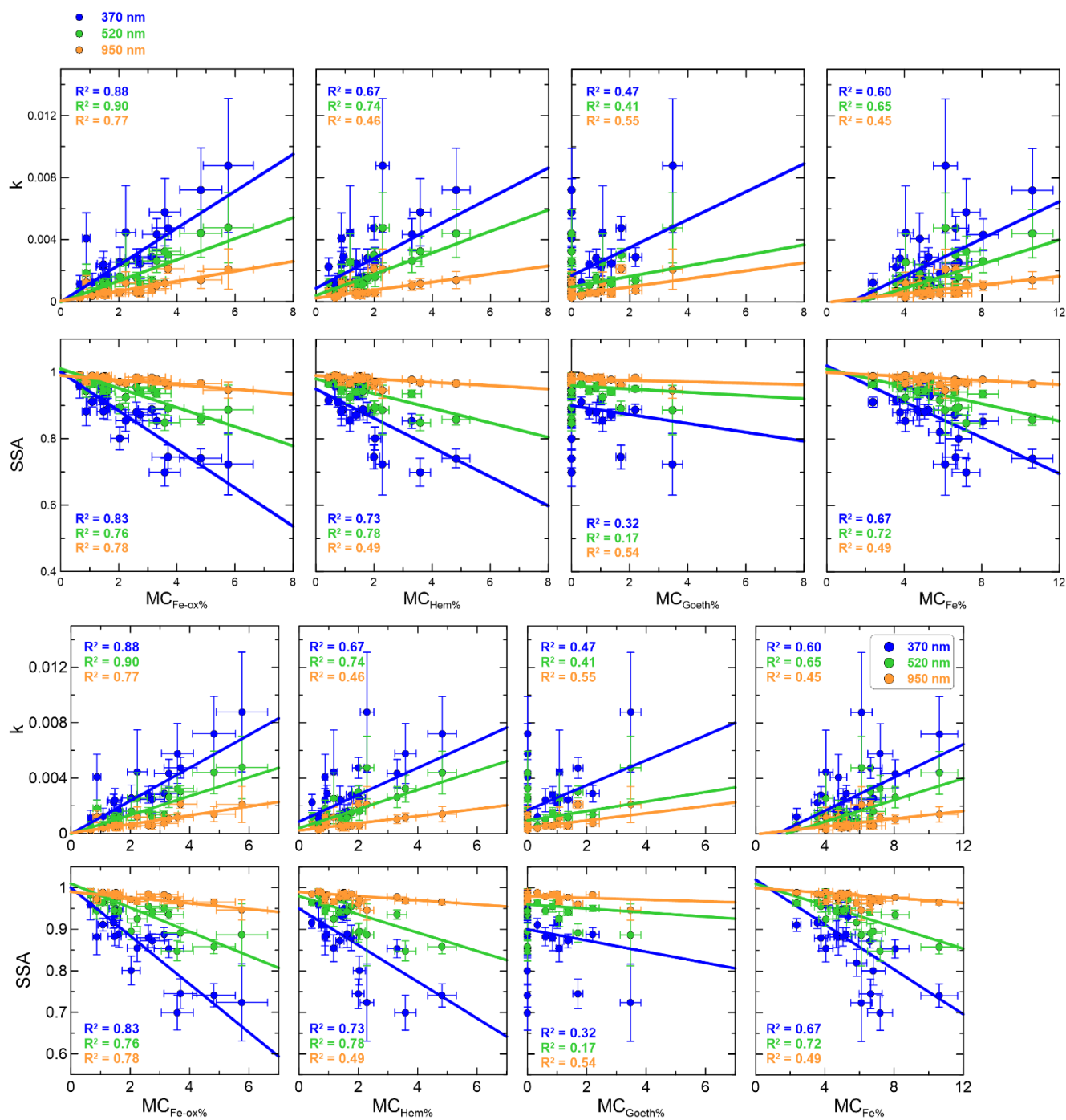
a)

b)
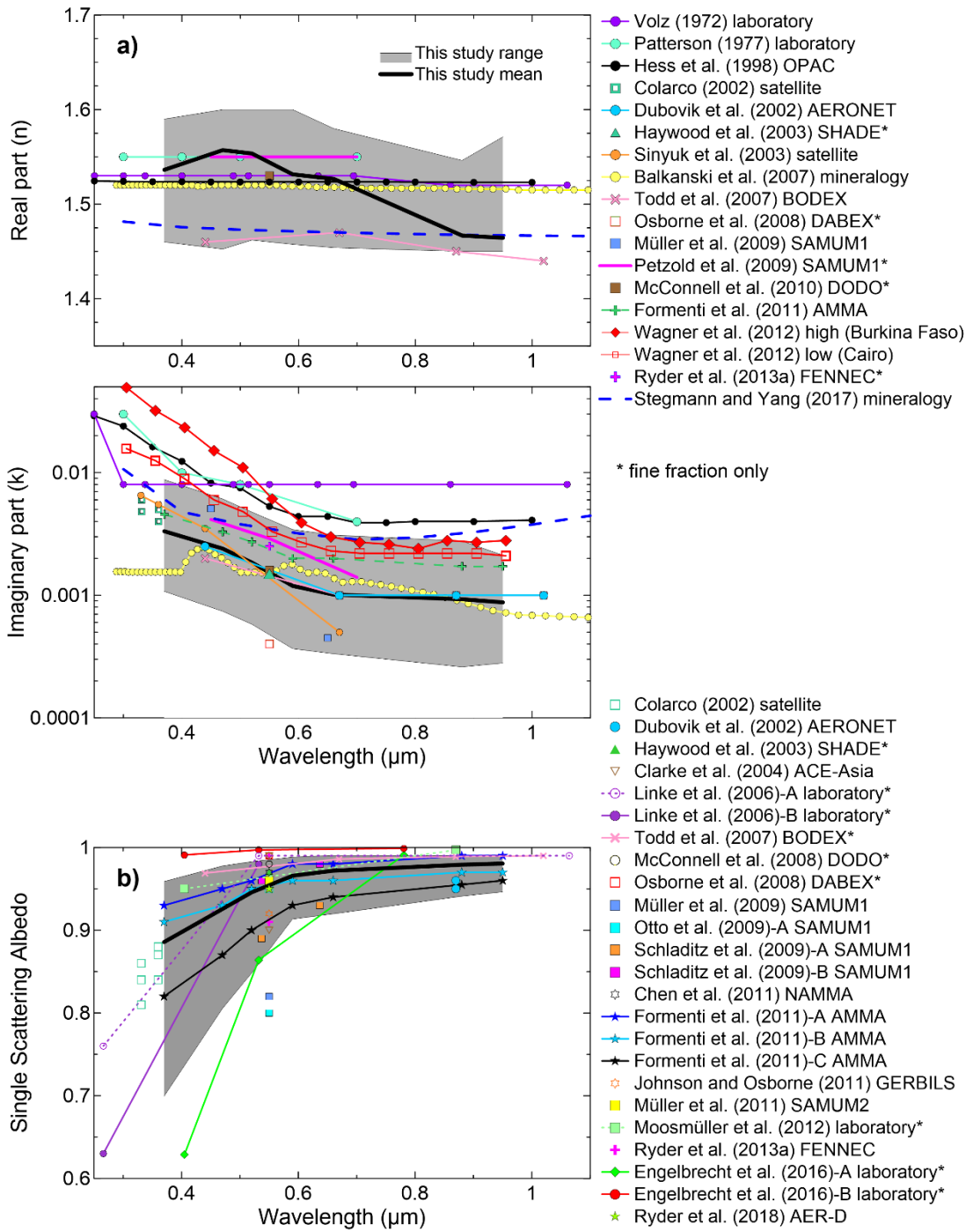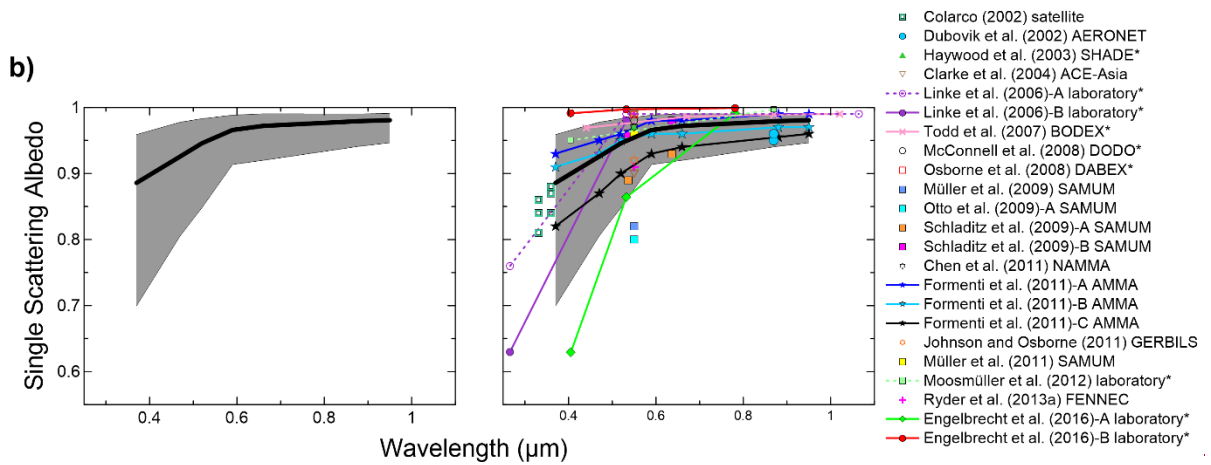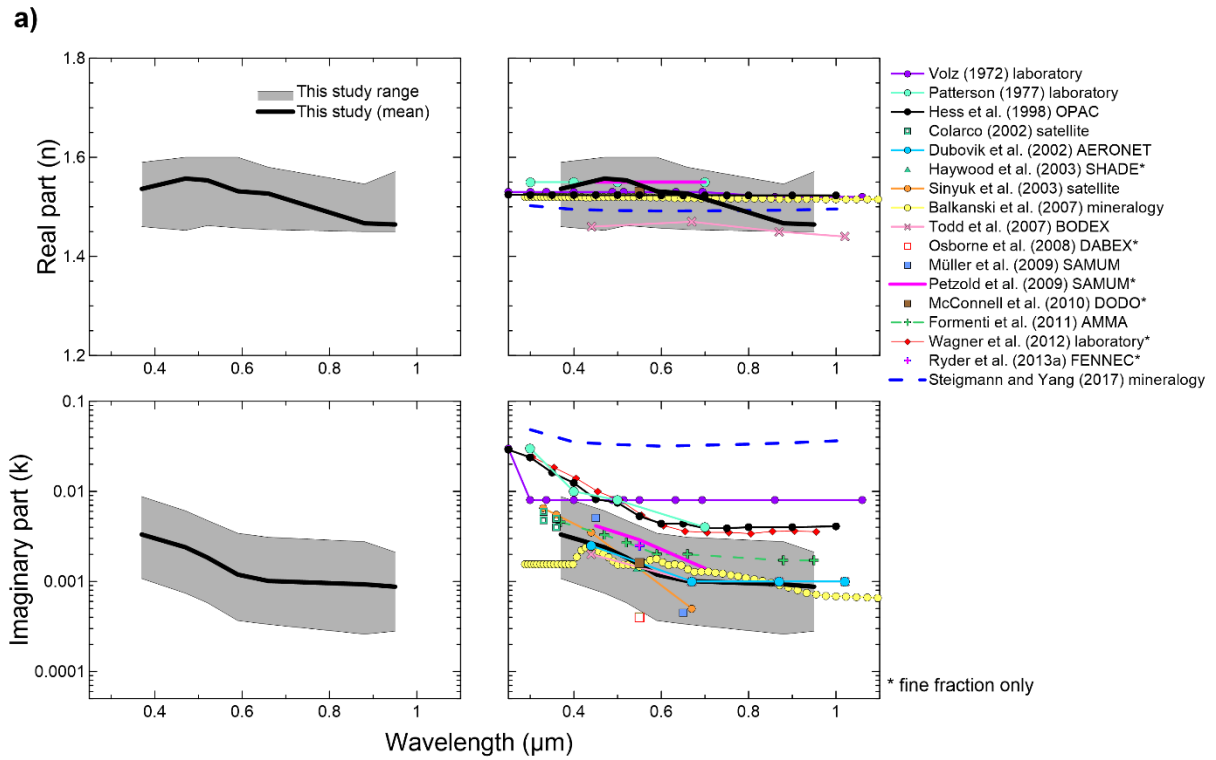
Figure 98. Experiment–averaged imaginary part of the refractive index (k, top panels) and single scattering albedo (SSA, bottom panels) at 370, 520, and 950 nm versus the mass concentration of iron oxides ($MC_{Fe-ox\%}$), hematite ($MC_{Hem\%}$), goethite ($MC_{Goeth\%}$), and elemental iron ($MC_{Fe\%}$) measured for the different dust samples analysed in this study. The calculated linear fit regression lines are shown, together with the correlation coefficients of the fits (R^2). The legend indicates the line styles used in the plots. Data for the Taklimakan sample were excluded from the k and SSA plots versus $MC_{Fe-ox\%}$, $MC_{Hem\%}$, and $MC_{Goeth\%}$ due to the absence of data for this sample.
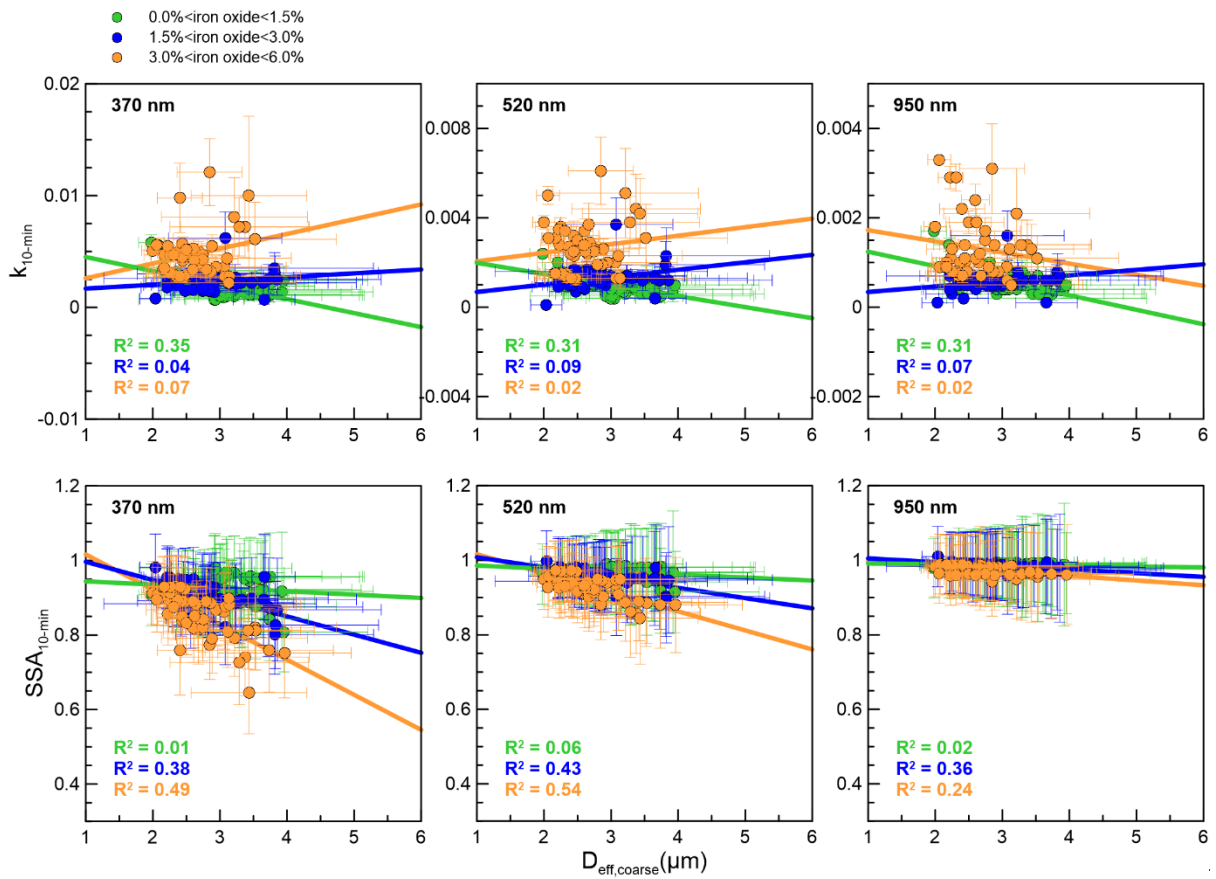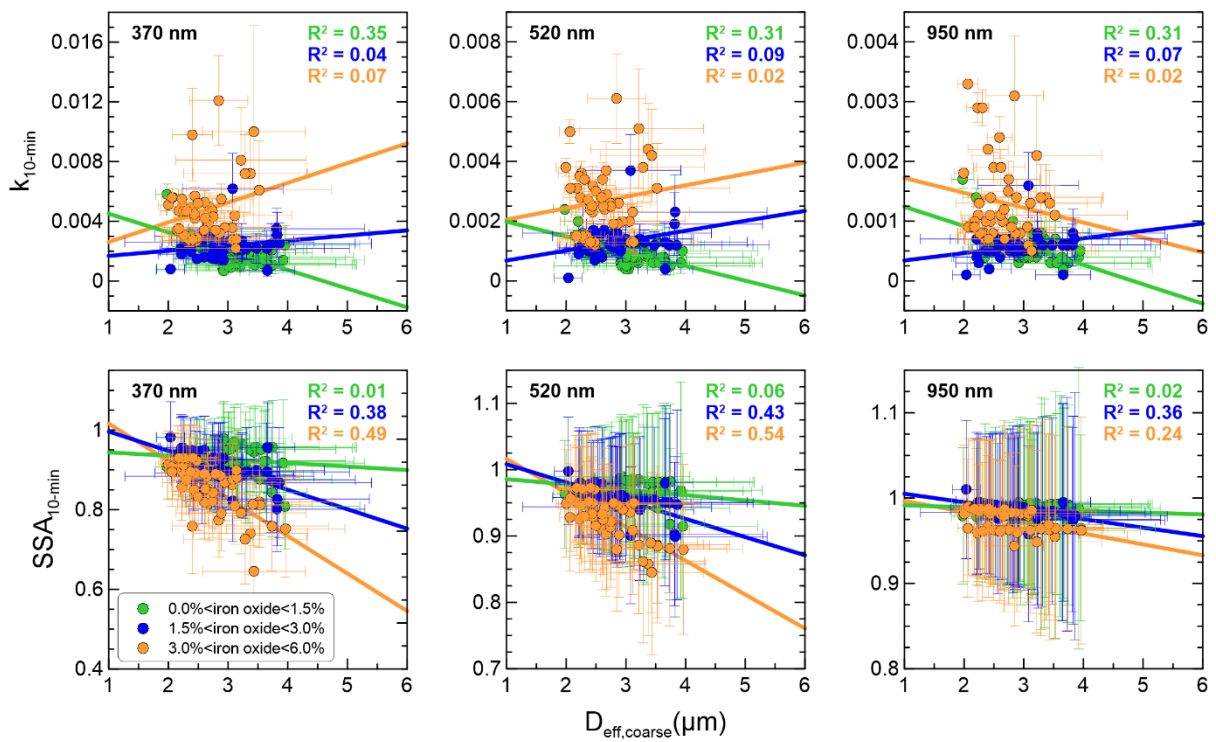
1525

1526

1527

1528

1529

1530

1531

1532

1533

1534

1535

1536

1537

1538

1539

1540

1541

1542 **Figure 109.** 10–min averaged imaginary refractive index (k_{10-min}, top panels) and single scattering al-

1543 bedo (SSA_{10-min}, bottom panels) at 370, 520, and 950 nm versus effective coarse diameter ($D_{eff,coarse}$)

1544 estimated at the input of the SW instruments. Data were classified in three classes based on the iron

1545 oxide content of the dust samples. The linear fit curves and the correlation coefficients for the linear

1546 regression fits for each dataset are also reported. The legend identifies the line styles used in the plots.

1547

1548

1551